

**IMPURITY QMC CALCULATIONS OF PERSISTENT
CURRENTS**

IMPURITY QUANTUM MONTE CARLO CALCULATIONS OF PERSISTENT CURRENTS

By

PETER HITCHCOCK, B.Arts Sc.

A Thesis

Submitted to the School of Graduate Studies
in Partial Fulfillment of the Requirements
for the Degree
Master of Science

McMaster University

©Copyright by Peter Hitchcock, 2006.

MASTER OF SCIENCE (2006)
(Physics)

McMaster University
Hamilton, Ontario

TITLE: Impurity Quantum Monte Carlo Calculations of Persistent Currents

AUTHOR: Peter Hitchcock, B.Arts Sc.(McMaster University)

SUPERVISOR: Dr. Erik S. Sørensen

NUMBER OF PAGES: vii, 53

Abstract

Recent interest in the fundamental physics of the Kondo effect has been driven by the observation of Kondo physics in mesoscopic systems such as quantum dots [1, 2] and carbon nanotubes [3], which can act analogously to magnetic impurities in a bulk metal. Highly tunable mesoscopic systems such as these present the possibility of observing the controversial Kondo length scale ξ_K associated with the cloud of conduction electrons that screen the spin of the impurity [4]. This plays a similar role in scaling theories as the Kondo temperature T_K .

One proposal [5] for detecting this length scale is to measure the finite-size dependence of persistent currents in an isolated conducting ring coupled to a quantum dot. The screening cloud should be ‘trapped’ in the closed system, and will not form if the size of the ring L is much smaller than ξ_K . In particular, the current in the Kondo regime should be a universal scaling function $j = L^{-1}f(\Phi, L/\xi_K, T/T_K)$ (here Φ is the applied flux) [6, 7]. Considerable disagreement has arisen in the theoretical estimates of these persistent currents as different analytical treatments yield contradictory predictions [6, 8, 9, 10].

This thesis presents a new Quantum Monte Carlo (QMC) technique for measuring persistent currents in such systems, based on the Hirsch-Fye Impurity QMC algorithm [11] which is ideally suited to treating systems with a single impurity such as the quantum dot. The algorithm provides exact numerical results at finite temperatures. The complexity of the algorithm does not scale directly with the size of the system, making it particularly attractive for investigating a wide range of system sizes.

Acknowledgements

To my supervisor, Dr. Erik Sørensen, I would like to extend my sincere appreciation for his guidance and support throughout my time at McMaster. I would like to thank him as well for putting up with my at times truant behaviour and for encouraging me to attend such enriching conferences.

During the four months I spent visiting the Department of Physics at UBC in Vancouver at which this project took form, I could not have asked for more welcoming hosts than Dr. Ian Affleck, his postdocs Nicolas Laflorencie and Jestko Sirker, and his graduate students Ming-Shyang Chang, Rodrigo Pereira, and Justin Malecki. I am privileged to have had the opportunity to interact with such an excellent group.

Thanks to my office mates Laura Filion and Kiri Nichol for their ever-educational distractions.

I am grateful to Dr. Catherine Kallin for her perpetual support in my scholarship and PhD applications. I have valued her candid advice in the course of my studies.

This thesis could not have been completed without the love and support from my partner Julia Croome. I apologize for putting our relationship through the trials of the academic path.

Finally I thank my father, Dr. Adam Hitchcock, for sharing with me his sense of wonder and delight in the scientific endeavour.

Contents

1	Introduction	1
1.1	Background	1
1.2	The Kondo Effect	2
1.3	Quantum Dots	4
1.4	Persistent Currents	6
1.5	Persistent Currents Through Quantum Dots	9
2	Hirsch-Fye Impurity QMC	13
2.1	Formalism	13
2.1.1	Discrete Hubbard-Stratonovich Transformation	14
2.1.2	Dyson Equation	17
2.1.3	The Monte Carlo Algorithm	18
2.2	Observables and Wick's Theorem	21
2.3	The Fermion Sign Problem	22
2.4	Complexity	23
3	Non-Interacting Persistent Current	25
3.1	The Current Operator	26
3.2	Embedded Quantum Dot	27
3.2.1	Imaginary-Time Green's Function (ITGF) Approach	27
3.2.2	Gogolin and Prokof'ev (GP) Approach	29
3.2.3	Single-particle Exact Diagonalization (ED) Approach	30
3.3	Side Coupled Quantum Dot	30

3.3.1	ITGF Approach	30
3.3.2	GP Approach	31
3.3.3	ED Approach	32
3.4	Results	32
3.4.1	Finite Temperature Effects	32
3.4.2	L even	34
3.4.3	L odd and Ensemble Effects	37
3.5	Conclusions	39
4	Interacting Persistent Current	41
4.1	Calculating the Current in the Hirsch-Fye Algorithm	41
4.2	Results	43
5	Conclusions and Perspectives	47
5.1	Conclusions	47
5.1.1	Accessible Parameter Regimes	47
5.2	Further Work	48

List of Figures

1.1	Energy levels and persistent current of an ideal ring	7
1.2	Commonly studied quantum dot ring geometries	10
3.1	Persistent current at finite temperature	33
3.2	Persistent current of a 16-site ring with an embedded quantum dot	34
3.3	Energy levels and persistent current of a ring weakly coupled to an impurity	35
3.4	Persistent current of a 16-site ring side-coupled to a quantum dot	36
3.5	L dependence of the current in the SCQD geometry at $\epsilon_d = 0$ with fixed N	36
3.6	Energy levels and persistent current of an ideal ring with odd L	38
3.7	Persistent current of a 17-site EQD	39
3.8	Persistent current of a 17 + 1-site SCQD	40
4.1	Extrapolation to $\Delta\tau = 0$ correcting for error due to Trotter decomposition	42
4.2	Persistent current of a 16-site ring with an embedded quantum dot at $U = 2$, comparison to $T = 0$ exact diagonalization results	43
4.3	Persistent current of a 16-site ring with an embedded quantum dot at $U = 0.5$ comparing to finite T approximate results . . .	44
4.4	Persistent current for a 16-site ring with an embedded quantum dot as a function of ϵ_d showing Coulomb blockade-like physics	45

Chapter 1

Introduction

1.1 Background

The impact of magnetic impurities on a bath of conduction electrons has captured the interest of generations of condensed matter physicists. The study of the seemingly straightforward physics of the Kondo problem has played an important role in the development of a number of fundamental tools in condensed-matter theory, including ideas of scaling and the renormalization-group (RG) approach. Despite the wealth of theoretical techniques [12, 13] that have been applied to the problem, fundamental interest continues due in no small part to relatively recent developments that allow various aspects of the physics to be investigated with a great deal of experimental control [1, 2, 14].

In particular, scaling theories of the Kondo problem predict the emergence of a characteristic length scale ξ_K (along with a characteristic energy scale T_K , the Kondo temperature) associated with a ‘cloud’ of conduction electrons that screen the spin of the magnetic impurity. Despite the fundamental role this length scale plays in theoretical treatments, experimental signatures of the screening cloud have to date never been seen [4, 15] and its existence has sometimes been questioned [16]. The large size of this cloud ($\approx 0.1\mu\text{m}$ in typical metals) is held to be responsible for this absence of experimental confirmation. The fine degree of control over the mesoscopic systems in which Kondo effects have recently been observed have rekindled hope that the screening cloud can finally be detected.

One candidate system for demonstrating the existence of this screening cloud is that of a small, isolated, conducting ring coupled to a quantum dot. Threading such a ring with a magnetic flux can induce persistent currents in thermodynamic equilibrium due to the Aharonov-Bohm effect; however, the Kondo physics associated with the quantum dot can strongly enhance or suppress these currents, depending on the particular details of the geometry. Specifically, the isolated nature of the rings ‘traps’ the Kondo screening cloud,

implying that the ratio of the size of the ring L to the size of the screening cloud ξ_K should have a strong impact on the behaviour of the system. Since such persistent currents have been observed in GaAs/GaAlAs heterostructures [17] similar to those in which the mesoscopic Kondo effect has also been observed [1], there is some hope that such a finite-size effect will be observable.

Consequently, considerable theoretical effort [5, 6, 8, 9, 10, 18, 19, 20, 21, 22, 23] has been invested in calculating the persistent current and its dependence on the length of the ring. Some disagreement has arisen as vastly contradictory results have been predicted by different analytical techniques. In lieu of this controversy, it is useful to consider numerical techniques that can provide essentially exact results in the relevant parameter regimes. To this end, this thesis describes a novel Quantum Monte Carlo (QMC) technique for numerically calculating properties of such systems, based on the Hirsch-Fye Impurity QMC algorithm [11].

The outline of this thesis is as follows. A brief history of the Kondo problem is presented in Sec. 1.2. The prediction and subsequent observation of Kondo physics in mesoscopic systems such as quantum dots is elaborated upon in Sec. 1.3. The physics of mesoscopic persistent currents in ideal conducting rings is introduced in Sec. 1.4, along with a brief review of the relevant experimental work. The theoretical controversy surrounding the effects of quantum dots on persistent currents is outlined in Sec. 1.5. Chapter 2 outlines in detail the theoretical framework of the Hirsch-Fye Impurity QMC algorithm. Chapter 3 presents calculations of the persistent current in the non-interacting Anderson-model which act as an input for the QMC; the current is calculated using several methods to confirm the results. In addition, this chapter serves to elaborate on the remarkably rich physics of persistent currents, even in non-interacting systems. Chapter 4 discusses the extensions needed in order to calculate the effects of interactions on persistent currents in the Hirsch-Fye algorithm and validates the technique by comparing the current as calculated by the described QMC algorithm with results from exact diagonalization and previously published perturbative results. Finally, Chap. 5 presents conclusions and perspectives on novel calculations that can be performed with this technique.

1.2 The Kondo Effect

Anderson and Kondo Impurities

The Kondo effect is one of the major paradigms of condensed matter theory. This introductory discussion is based on the textbook by Hewson [12]. The effect was first associated with the upturn in the low-temperature resistance of

metals doped with magnetic impurities (i.e. those exhibiting a Curie term in the magnetic susceptibility, indicating the presence of free spins). Two simple models of isolated impurities in a bath of conduction electrons have played important roles: the Anderson model and the Kondo model. The Anderson model emphasizes the strong repulsive Coulomb interaction present in the d-orbitals of magnetic impurities and in its simplest form it treats the impurity as a single localized orbital. In second-quantized form, the Hamiltonian reads

$$H_{AM} = \sum_{k,\sigma} \epsilon_k \hat{c}_{k\sigma}^\dagger \hat{c}_{k\sigma} + \sum_{k,\sigma} [V_k \hat{c}_{k\sigma}^\dagger \hat{c}_{d\sigma} + \text{H.c.}] + \sum_{\sigma} \epsilon_d \hat{c}_{d\sigma}^\dagger \hat{c}_{d\sigma} + U \hat{n}_{d\uparrow} \hat{n}_{d\downarrow}. \quad (1.1)$$

Here $\hat{c}_{k\sigma}$ ($\hat{c}_{k\sigma}^\dagger$) are annihilation (creation) operators for electrons in state k with spin σ , $\hat{n}_{d\sigma} = \hat{c}_{d\sigma}^\dagger \hat{c}_{d\sigma}$ is the number operator for electrons in the impurity orbital with spin σ , ϵ_k and ϵ_d are the single-particle energies of the conduction and impurity states, respectively, V_k is the hybridization, and U is the Coulomb interaction.

In the limit that the impurity is singly-occupied ($\epsilon_d \ll \epsilon_F \ll \epsilon_d + U$), the Anderson model reduces to the Kondo or s-d model via a Schrieffer-Wolff transformation. The Kondo model treats the impurity as a localized spin operator \vec{S}_d interacting with the conduction electrons via a magnetic exchange interaction J , suppressing the particle-number fluctuations present in (1.1)

$$H_K = \sum_{k,\sigma} \epsilon_k \hat{c}_{k\sigma}^\dagger \hat{c}_{k\sigma} + \sum_{k,k'} J_{kk'} \hat{c}_k^\dagger \frac{\vec{\sigma}}{2} \hat{c}_{k'} \cdot \vec{S}_d \quad (1.2)$$

where $\vec{\sigma}$ are the Pauli matrices.

The Kondo coupling generated by the Schrieffer-Wolff transformation, in terms of the parameters of the Anderson model, is

$$J_{kk'} = V_k^* V_{k'} \left(\frac{1}{\epsilon_k - \epsilon_d} + \frac{1}{U + \epsilon_d - \epsilon_{k'}} \right) \quad (1.3)$$

Typically an isotropic coupling $J_{kk'} = J$ is considered.

Particle-Hole Symmetry

Assuming a dispersion relation ϵ_k and hybridization V_k that are sufficiently symmetric about the Fermi level ϵ_F (which will be set to $\epsilon_F = 0$ for the purposes of this thesis), the Anderson impurity is particle-hole symmetric at the single point $-\epsilon_d = U/2$. This corresponds to half-filling. The Kondo impurity is particle-hole symmetric at half-filling.

The Kondo Resonance and Screening Cloud

Standard perturbation theory is not sufficient to describe the low temperature behaviour of magnetic impurities, as perturbative approaches in these simple models generate terms logarithmic in the temperature that diverge as $T \rightarrow 0$. Proper understanding of the physics of such impurities below the characteristic Kondo temperature T_K requires ideas of scaling and the renormalization group. The general picture that emerges is that at sufficiently low temperatures, scattering of conduction electrons off the impurity spin becomes strongly correlated. The impurity spin forms a singlet with a ‘cloud’ of conduction electrons which then screens the spin. Associated with this cloud is a sharp resonance (of width T_K) in the conduction electron density of states fixed to the Fermi level ϵ_F , called the Kondo resonance. Although T_K depends (sometimes strongly) on the particular parameters of the model, below this temperature it becomes the *only* relevant energy scale and all thermodynamic properties of the system become universal functions of T/T_K . In bulk metals, the Kondo resonance enhances scattering off of the magnetic impurities, leading to the characteristic upturn of the resistance as $T \rightarrow 0$. Concepts of scaling and universality have been confirmed experimentally, and by numerous theoretical techniques [12].

A further consequence of the renormalization group approach to the Kondo effect is that the screening cloud should have a characteristic length scale, $\xi_K \approx \hbar v_F / k_B T_K$, which is on the order of $0.1 \mu\text{m}$ in most metals. In the strong-coupling limit, this length scale should be the only relevant one, akin to T_K for thermodynamic functions. Hence spatial correlations should be universal functions of r/ξ_K [4, 15]. This length scale, however, has never been observed experimentally, and some controversy exists over its theoretical validity [16].

1.3 Quantum Dots

Recent developments in nano-fabrication have allowed experimentalists to construct conducting devices small enough to see discrete electron energy levels. It was suggested [24, 25] that if one could prepare a mesoscopic device (such as a quantum dot) with a localized spin, Kondo physics should become relevant below a certain T_K . Clear evidence of the mesoscopic Kondo effect was first seen in a semiconductor quantum dot by Goldhaber-Gordon *et al.* in 1998 [1], confirmation of which followed soon after from Cronenwett, Oosterkamp and Kouwenhoven [2], Schmid *et al.* [26], Van der Wiel *et al.* [14] and others.

Semiconductor quantum dots used to investigate the mesoscopic Kondo effect are typically constructed on the two-dimensional electron gas (2DEG) formed at the interface of GaAs/GaAlAs hetero-layers. Metallic features can be patterned on top of the 2DEG allowing experimental structures to be de-

ned. Quantum dots are formed by isolating a small region ($\sim 150 \text{ nm}^2$ in the Goldhaber-Gordon experiment) of the 2DEG. Often three gates are used whose relative potential can be tuned: two to control the coupling of the dot to surrounding conduction electrons, and the third to control the number of electrons on the dot itself. The small dimensions of the dot lead to large, discrete energy spacings $\delta\epsilon$. Doubly-occupying a single state with two electrons (of opposite spin) is associated with a repulsive Coulomb energy U . These energy scales can be clearly detected by measuring the differential conductance $G = dI/dV$ through the quantum dot as a function of the gate voltage ϵ_d , due to Coulomb blockade physics.

Coulomb Blockade and Kondo Enhancement of the Conductance

At low temperatures, transport through the dot occurs only at energies between the Fermi-levels of the source and drain leads, μ_L and μ_R [27]. If the resonances associated with the energy levels of the dot are separated and narrow enough (as defined by the size of the dot and strength of the couplings between the dot and the leads) that the Fermi levels lie between two resonances, the number of electrons on the dot cannot fluctuate and transport is forbidden. This is the Coulomb blockade. A typical measurement of G as a function of the gate voltage finds a sequence of peaks as ϵ_d passes resonances in the dot density of states separated by valleys in which the conductance is strongly suppressed.

When the dot is occupied by an odd number of electrons, however, it acts as a localized spin. A Kondo resonance forms at temperatures below [28]

$$T_K \approx \sqrt{U\Gamma} e^{-\pi(\mu - \epsilon_0)/2\Gamma}. \quad (1.4)$$

Here Γ is the broadening of the dot energy levels and ϵ_0 is the energy of the highest occupied level. This resonance allows electrons to tunnel through the dot, enhancing the conductance in the region suppressed by the Coulomb blockade. The characteristic sequence of valleys in the conductance as a function of gate voltage can thus be divided into two alternating types; those in which the dot is evenly occupied in which the conductance drops with T , and those with odd occupancy in which the conductance begins to increase once T drops below T_K .

Kouwenhoven's group later demonstrated the striking fact that the Kondo enhanced conductivity could reach the unitary limit (the theoretical maximum for single-channel conductors), completely overcoming the Coulomb blockade [14]. The ability to tune the conductance so strongly may have important technological applications.

Another experiment by Goldhaber-Gordon *et al.* explored the mixed-valence regime of the Anderson model, confirming that semi-conductor quan-

tum dots are well described by the Anderson Hamiltonian [29]. Further work has demonstrated the Kondo effect in a variety of other mesoscopic systems, including spin-1 quantum dots [30], carbon nano-tubes [3] and multiple quantum dot systems [31, 32].

The fine control available over quantum dots should allow for investigations into many fundamental aspects of Kondo physics that are not directly observable in bulk metallic systems. In order to observe the screening cloud, the theoretical goal is to describe an experimentally observable quantity whose behaviour clearly demonstrates the Kondo length scale ξ_K . One suggestion that has received considerable theoretical attention is the persistent current in a conducting loop coupled to a quantum dot, which should show evidence of finite size effects when the conducting loop is smaller than the Kondo screening cloud.

1.4 Persistent Currents

Persistent Currents in Ideal Rings

Circulating currents generated by an Aharonov-Bohm flux¹ Φ that remain stable in thermodynamic equilibrium were first investigated in superconducting rings, in which the current serves to quantize the flux passing through the ring in units of $\Phi_s = ch/2e$ (see [33] for instance). However, it was pointed out by Büttiker and others [34] that such flows could be expected in normal metal rings as well, provided that the phase of the conduction electron remained coherent as it circuited the ring. The essential observation was that this would not require a perfect sample: so long as the impurities and other scattering centres are static on the time scale of a single circuit, the phase shift of the electrons remains coherent and the Aharonov-Bohm twist should result in finite current flow. Further discussion of the concept of a decoherence time can be found in the textbook by Imry [35], amongst others.

The Aharonov-Bohm flux induces a complex twist in the electron wave functions. The vector potential can be gauge-transformed into the boundary conditions

$$\Psi(x + L) = \Psi(x)e^{i\alpha}, \quad \alpha = 2\pi\Phi/\Phi_0 \quad (1.5)$$

where $\Phi_0 = ch/e$ is the flux quantum (about 4.136×10^{-15} Wb) and L is the length of the ring (measured, for the purposes of this thesis, in units of the lattice constant a). Since the wave functions are thus periodic functions of Φ , it follows that all properties of the system (including the persistent current) must also be periodic in Φ . Moreover, the current density can be calculated

¹An Aharonov-Bohm flux threads the interior of a ring without applying a field at the sites of the ring itself.

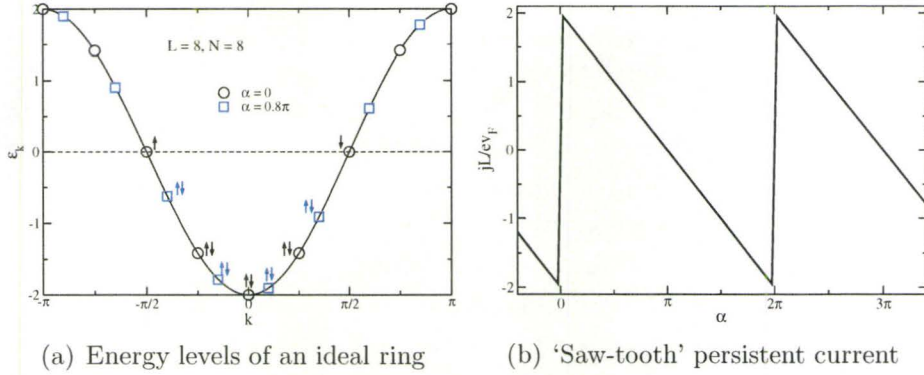


Figure 1.1: (a) Energy levels of an 8-site tight-binding ideal ring at $\alpha = 0$ and $\alpha = 0.1\pi$. The number of electrons occupying each state is indicated by the arrows. The allowed wave vectors shift to the right as α increases. The current density $-ev_n/L$ carried by the right- and left-moving states cancels exactly at $\alpha = 0$ (circles). The degeneracy at the Fermi-level is broken by a small applied flux (squares) upon which the highest-occupied left-moving state becomes doubly occupied. (b) The normalized persistent current jL/ev_F for the same ring. The current is linear in the flux and jumps discontinuously at $\alpha = 2n\pi$.

by taking the derivative of the ground state energy (at zero temperature) or the free energy (at finite temperature) with respect to the flux

$$j = -c \frac{dE_0}{d\Phi} = -\frac{e}{\hbar} \frac{dE_0}{d\alpha}. \quad (1.6)$$

It is reasonably straightforward to calculate the persistent current for non-interacting electrons at $T = 0$ in an ideal ring (considering a single orbital at each site with no defects or disorder off of which the electrons can scatter). This problem has been discussed lucidly and extensively by Cheung *et al.* [36].

From Eq. (1.5), we can see that the only effect of the flux will be to modify the allowed wave vectors in the system

$$k_n = \frac{2\pi n}{L} + \frac{\alpha}{L}, \quad n = 0, \dots, L-1. \quad (1.7)$$

For a quadratic dispersion relation $\epsilon_k = \hbar^2 k^2 / 2m$ with fixed particle number, the ground state energy will be quadratic in the flux as well and thus the persistent current will be linear in the flux. Using a tight-binding Hamiltonian

$$H = t \sum_{\substack{j=0 \\ \sigma}}^{L-1} \hat{c}_{j\sigma}^\dagger \hat{c}_{j+1\sigma} + \hat{c}_{j+1\sigma}^\dagger \hat{c}_{j\sigma}, \quad (1.8)$$

and the corresponding dispersion relation $\epsilon_k = -2t \cos k$, the current converges on the same result very quickly as L increases. Figure 1.1(a) shows the tight-binding dispersion relation and the allowed wave-vectors for an 8-site ring at two values of α . At half-filling there will be $N = L$ electrons in the ring. When there is no applied flux, the current carried by the occupied right-moving and left-moving states will cancel exactly. When a flux is applied this symmetry between right and left moving states is broken, but to a good approximation the current is dominated by the contribution of the highest occupied state. Thus when a small positive flux is applied, the left-moving state just below the Fermi level becomes doubly occupied, leading to a current of order $j \approx e\hbar\pi/mL^2 = 2ev_F/L$. The current decreases linearly with α until the highest occupied right-moving state crosses the Fermi level at $\alpha = 2n\pi$ upon which the current jumps discontinuously back to $j = 2ev_F/L$. This characteristic ‘saw-tooth’ wave is shown in Fig. 1.1(b).

It must be stressed that the amplitude and periodicity of this saw-tooth is strongly dependent on the parity of the ring L and the number of electrons N . At half-filling for L even, the current is 2π periodic in α (this corresponds to a ϕ_0 periodicity in the flux); however the phase of the current is shifted by π when $L/2$ is odd (that is, for a 10-site ring the discontinuities in the current occur at $\alpha = (2n + 1)\pi$ rather than at $\alpha = 2\pi$ as they do for the $L = 8$ ring). Defining $[\theta]$ between $-\pi$ and π by

$$\theta = 2n\pi + [\theta] \quad (1.9)$$

the current for L even is

$$j = \begin{cases} -\frac{2ev_F}{\pi L}[\alpha - \pi], & L/2 \text{ even} \\ -\frac{2ev_F}{\pi L}[\alpha], & L/2 \text{ odd.} \end{cases} \quad (1.10)$$

For L odd there is only a single electron in the highest occupied state. The maximum magnitude of the saw-tooth curve is thus only ev_F/L and it becomes π periodic in α ($\phi_0/2$ periodic in the flux)

$$j = -\frac{ev_F}{\pi L}([\alpha] + [\alpha - \pi]), \quad L \text{ odd.} \quad (1.11)$$

The persistent current, however, is very sensitive to many specific details of the Hamiltonian considered, making it difficult to accurately predict the outcome of experiments. Lévy *et al.* [37] reported the first observation of persistent currents in an ensemble of 10^7 copper rings, with an area of $0.3 \mu\text{m}^2$, cooled to as low as 10 mK. They observed a $\Phi_0/2$ periodicity in the current, which was attributed to the ensemble average washing out the first

harmonic. Chandrasekhar *et al.* performed a similar experiment [38] on a single gold loop of similar dimension to the copper rings in Ref. [37]. They observed the expected Φ_0 periodicity but found the magnitude of the current to be nearly two orders of magnitude larger than theoretical predictions. Mailly and coworkers performed experiments [17, 39] on semi-conductor loops in a GaAs/GaAlAs hetero-structure, similar to those used for quantum dot experiments. Their observations matched the theory closely, but the lower carrier density (thus stronger interaction effects) and weak disorder of the semi-conductor loop called into question theoretical explanations of the current in metallic rings based on the effects of interaction and disorder. Further experiments on arrays of gold rings [40], connected semi-conductor rings [41] and silver rings [42] investigated diffusive effects, connectivity of multiple rings, and spin-orbit coupling (respectively). Experiments on persistent currents are very difficult to perform, and observations can only be made of the first few harmonics of the current rather than the full detailed flux dependence.

1.5 Persistent Currents Through Quantum Dots

No experiment has been done to date that has observed the effect on persistent currents of coupling the conducting loops to a quantum dot; indeed it has been suggested that this would be an extremely challenging experiment. Theoretically, however, such persistent currents have received much attention.

When considering the effects of quantum dots on persistent currents, two geometries are commonly considered. In the first (Fig. 1.2(b)), the quantum dot is embedded directly in the conducting loop such that conduction electrons must pass through the dot in order to complete the circuit; this is referred to as the Embedded quantum dot (EQD). The dot is coupled to the ring by a modified tunnelling constant t' . In the second, the quantum dot is coupled to the side of the ring (also with a modified tunnelling constant t') such that the current is affected primarily by the strong correlations between the dot and the ring; this is referred to as the Side-Coupled quantum dot (SCQD). The dots can be modelled either as an Anderson impurity or the simpler Kondo impurity. This thesis will focus exclusively on the Anderson impurity models since they are more naturally suited to the Hirsch-Fye impurity QMC approach. The specific Hamiltonians studied will be presented in Chap. 3.

Much of the controversy regarding the persistent current when the ring is coupled to a quantum dot surrounds the effects of the finite size of the ring. Two opposite limits are considered. In the first the ring is much larger than the size of the screening cloud $L \gg \xi_K$ or equivalently the level spacing in the ring is much larger than the Kondo temperature $\delta\epsilon \gg T_K$. In the second, the

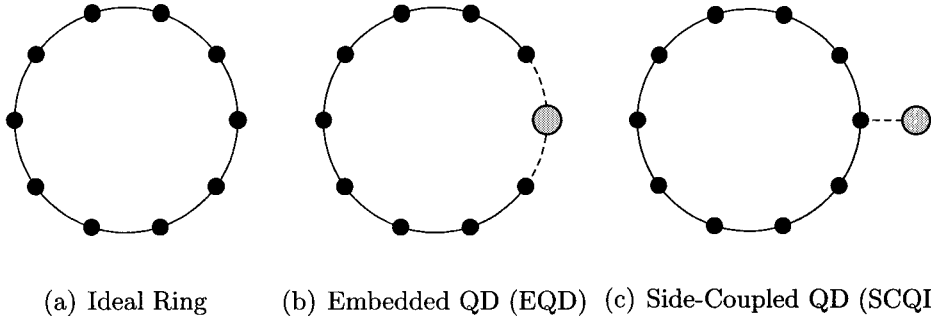


Figure 1.2: Commonly studied geometries for considering the effects of quantum dots on persistent currents. (a) A tight-binding, ideal ring. Coulomb interactions are neglected. The quantum dots in (b) and (c) are indicated by the large grey site. The dots are typically modelled either as a Kondo or an Anderson impurity. In all three systems shown the number of sites in the ring L is 10, but the number of electrons N at half-filling is one greater for the SCQD geometry ($N = 11$) than for the ideal ring and EQD geometries ($N = 10$).

ring is taken to be much smaller than the screening cloud $L \ll \xi_K$ ($\delta\epsilon \ll T_K$). The behaviour of the current with the dot is usually discussed relative to the ideal case.

Büttiker and Stafford considered [8] both geometries in the limit $L \ll \xi_K$, assuming no Kondo effects will be present in this limit. Working in the Anderson model, they studied the effects of charge transfer between the dot and the ring on the persistent current. In the EQD case, Coulomb blockade effects similar to those discussed earlier suppress the current except when a single-particle resonance from the dot passes through the Fermi level. In contrast, Coulomb blockade effects are not present in the SCQD case, but due to the strong effects of parity on the current, the transfer of electrons from the ring to the dot induces a strong change in the magnitude of the current.

Kondo effects were considered in the EQD by Ferrari *et al.* [18] in a cluster mean-field approach, pointing out that the Kondo resonance should give rise to a persistent current as $L > \xi_K$. Furthermore, they argued using slave-boson mean field theory that the current at the Kondo resonance should go as $O(1/\sqrt{L})$ (rather than as $O(1/L)$). Applying a variational ansatz to the EQD, Kang and Shin argued that parity effects suppress this Kondo enhancement for N odd [19].

The SCQD case was considered by Eckle *et al.* using a Bethe ansatz [9], by Cho *et al.* using slave-boson theory in the $U \rightarrow \infty$ limit with a diagrammatic expansion [20], by Anda *et al.* using a form of cluster mean-field theory [23], and by Zvyagin and Schlottmann, also using a Bethe ansatz [43]. These works

argued the Kondo effect should lead to an ideal current in the $L \gg \xi_K$ limit.

These predictions, however, were contradicted by Hu *et al.* using slave-boson mean field theory [21] and by Simon and Affleck, who developed a renormalization-group-enhanced perturbation theory [5, 6]. The latter argued that the current should in fact be a universal function of the flux and of the ratio ξ_K/L

$$jL = f(\alpha, \xi_K/L). \quad (1.12)$$

In the (strong-coupling) limit of $L \gg \xi_K$, the Kondo-coupling should renormalize to infinity, but in the opposite limit, $\xi_K \gg L$, the finite size provides an infrared cutoff bounding the growth of the renormalized coupling. In this limit, standard perturbation theory should apply. These works predicted that as a result of the Kondo resonance at half-filling, the persistent current in the EQD should be that of the ideal ring. On the other hand, the impurity in the SCQD should form a singlet with a localized conduction electron in the ring, leading to a complete suppression of the current. In the $L \ll \xi_K$ limit, low-harmonics of the current dominate leading to a sinusoidal current (suppressed from the ideal ‘saw-tooth’ curve).

These limits have been tested numerically by ED and DMRG techniques, which found good agreement with the small L perturbation approach and evidence supporting the predictions of strong coupling behaviour [10]. Perturbation theory in $1/J_K$ for the weak-coupling, SCQD case finds further evidence that $jL \rightarrow 0$ in this limit, though very large values of J_K were required to see good numerical agreement. The effects of particle-hole symmetry breaking off of half-filling remain unclear, though they are predicted to have a larger effect on the SCQD when N is odd [44].

Despite (or perhaps because of) the wide range of approaches applied to calculating the persistent current, there remains some controversy over its true behaviour, particularly in the strong-coupling limit of the SCQD where the effects of particle-hole symmetry breaking are unclear. While extensive numerical work has been done at zero temperature for smaller system sizes, the development of a Quantum Monte Carlo algorithm for calculating persistent currents in the two commonly considered geometries would be useful for confirming analytical predictions and understanding the behaviour in the cross-over region where $L \approx \xi_K$. The algorithm described in this thesis is ideally suited for calculation of the persistent current at finite temperatures which are more relevant to the experimental situation. In the context of the scaling theory, at finite temperatures the current should become a universal function of three arguments

$$jL = f(\alpha, \xi_K/L, T/T_K). \quad (1.13)$$

Chapter 2

The Hirsch-Fye Impurity Quantum Monte Carlo Algorithm

2.1 Formalism

The Hirsch-Fye impurity algorithm is ideally suited to treat fermionic systems in which the interactions are treated only in a small fraction of the system. Originally developed to investigate the single impurity Anderson model [11, 45], it has been used heavily as a component of Dynamic Mean Field Theory (DMFT) calculations [46]. While I am not aware of it having been used to calculate persistent currents through normal-metal, it has been used to investigate persistent currents through a Josephson-coupled superconducting ring.

The derivation of the algorithm relies on a discrete version of the Hubbard-Stratonovich transformation for Anderson impurity interaction terms $U\hat{n}_{d\uparrow}\hat{n}_{d\downarrow}$. While results can be obtained for Kondo impurities via a $U \rightarrow \infty$ projection technique [47], this thesis will focus on Anderson impurities. The Hirsch-Fye QMC algorithm is a finite-temperature algorithm; a related algorithm developed by Feldbacher, Held, and Assaad is better suited for obtaining zero-temperature results, and may be similarly applicable [48].

There are numerous reviews of the algorithm in the literature; the following is based largely on [45, 46, 49, 50]. This chapter is primarily a review of the algorithm, emphasizing the role of the impurity green's function. The non-interacting green's functions which act as input to the QMC are discussed in detail in Chap. 3, and some remaining details specific to calculating persistent currents are discussed in Chap. 4.

2.1.1 Discrete Hubbard-Stratonovich Transformation

We consider the Anderson model, broken up into interacting and a non-interacting parts

$$\hat{H}_{\text{AM}} = \hat{H}_0 + \hat{H}_I \quad (2.1)$$

$$\hat{H}_0 = \sum_{k,\sigma} \epsilon_k \hat{c}_k^\dagger \hat{c}_k + \sum_{k,\sigma} [V_k \hat{c}_{k\sigma}^\dagger \hat{c}_{d\sigma} + \text{H.c.}] + \sum_{\sigma} (\epsilon_d + \frac{U}{2}) \hat{c}_{d\sigma}^\dagger \hat{c}_{d\sigma} \quad (2.2)$$

$$\hat{H}_I = U \left[\hat{n}_{d\uparrow} \hat{n}_{d\downarrow} - \frac{1}{2} (\hat{n}_{d\uparrow} + \hat{n}_{d\downarrow}) \right]. \quad (2.3)$$

and the partition function

$$Z = \text{Tr} e^{-\beta \hat{H}_{\text{AM}}} = \text{Tr} \prod_{\ell=1}^{L_\tau} e^{-\Delta\tau(\hat{H}_0 + \hat{H}_I)}, \quad \Delta\tau = \frac{\beta}{L_\tau}. \quad (2.4)$$

At this point we apply the Trotter decomposition to separate the interacting and non-interacting parts of the Hamiltonian, which introduces a systematic error of $O(\Delta\tau^2)$ (one must be careful about the nature of \hat{H}_0 and \hat{H}_I here in order to ensure the linear error cancels [49, 51]).

$$Z = \text{Tr} \prod_{\ell=1}^{L_\tau} e^{-\Delta\tau \hat{H}_0} e^{-\Delta\tau \hat{H}_I} + O(\Delta\tau^2). \quad (2.5)$$

This is the only systematic source of error in the algorithm. The error remains finite in practise, since we work at finite L_τ , and it will be present in the estimates of all observables calculated. However, the limit of $\Delta\tau^2 \rightarrow 0$ can in practise be extrapolated. For brevity I will neglect this term in the remainder of this discussion.

The exponential term with the interacting part of the Hamiltonian can now be decomposed into quadratic terms by introducing an Ising-like auxiliary spin $\phi = \pm 1$. This can be done in a number of ways depending on which symmetry one wishes to respect in the resulting Hamiltonian [49, 52]. Here we will use a decomposition which breaks the $SU(2)$ symmetry of the system (it is restored upon integrating out the auxiliary spin), but which leads to a simpler final expression. Since the fermionic number operators can only take on the values 0 and 1,

$$e^{-\Delta\tau U \left[\hat{n}_{d\uparrow} \hat{n}_{d\downarrow} - \frac{1}{2} (\hat{n}_{d\uparrow} + \hat{n}_{d\downarrow}) \right]} = \frac{1}{2} \text{Tr}_\phi e^{\lambda \phi [\hat{n}_{d\uparrow} - \hat{n}_{d\downarrow}]}, \quad \cosh \lambda = e^{\Delta\tau U/2}. \quad (2.6)$$

Performing this transformation at every time-slice removes the interaction term at the cost of generating an effective time-dependant potential that acts

only at the impurity and depends on the auxiliary spins $\{\phi_\ell\}$. Since there are no terms that couple the two spin sectors, we can partition Z into a separate trace over each sector. Neglecting the constant pre-factor,

$$Z = \text{Tr}_{\{\phi_\ell\}} \prod_{\sigma} \text{Tr} \prod_{\ell=1}^{L\tau} e^{-\Delta\tau \hat{H}_0^\sigma} e^{\hat{V}_\ell^\sigma}, \quad (2.7)$$

where the effective time-dependent potential is given by

$$\hat{V}_\ell^\sigma = V_\ell^\sigma \hat{n}_{d\sigma}, \quad V_\ell^\sigma = \lambda\sigma\phi_\ell, \quad (2.8)$$

with $\sigma = \pm 1$.

The fermionic degrees of freedom can now be integrated out. The description of this procedure is strongly based on the nice discussion of Hirsch, in the Appendix of Ref. [53]. It is useful to re-label the fermion operators \hat{c}_α where α runs over all $L - 1$ conduction wave-vectors k and the impurity site d . The non-interacting Hamiltonian can thus be written in terms of an $L \times L$ matrix h_0

$$\hat{H}_0 = \sum_{\alpha,\beta} \hat{c}_\alpha^\dagger (h_0)_{\alpha\beta} \hat{c}_\beta \quad (= \hat{c} h_0 \hat{c}^\dagger). \quad (2.9)$$

Similarly the effective potential can be described by an $L \times L$ matrix at each time slice with a single non-zero element V_ℓ^σ .

The many-body trace is of the form

$$\text{Tr} e^{\hat{c}^\dagger A_1 \hat{c}} e^{\hat{c}^\dagger A_2 \hat{c}} \dots e^{\hat{c}^\dagger A_N \hat{c}}. \quad (2.10)$$

The trace can be evaluated straightforwardly with the identity

$$e^{\hat{c}^\dagger A \hat{c}} e^{\hat{c}^\dagger B \hat{c}} = e^{\sum_i \hat{\nu}_i^\dagger \lambda_i \hat{\nu}_i}, \quad (2.11)$$

where $\hat{\nu}_i$ are the single-particle basis states that diagonalize the matrix $e^A e^B$ and e^{λ_i} are its corresponding eigenvalues. This identity is established in detail by Hirsch in the Appendix of Ref. [53]. We can then evaluate the trace in the ν basis. Since each state can independently be occupied or unoccupied, the trace over the full 2^L many-body Hilbert space is

$$\begin{aligned} \text{Tr} e^{\hat{c}^\dagger A \hat{c}} e^{\hat{c}^\dagger B \hat{c}} &= \text{Tr} e^{\sum_i \hat{\nu}_i^\dagger \lambda_i \hat{\nu}_i} \\ &= \prod_i (1 + e^{\lambda_i}) \\ &= \det (I + e^A e^B). \end{aligned} \quad (2.12)$$

The last determinant is taken over the L spatial degrees of freedom.

Two definitions are convenient. Let

$$B_0 = e^{-\Delta\tau h_0}, \quad B_\ell^\sigma = B_0 e^{V_\ell^\sigma}. \quad (2.13)$$

These are $L \times L$ matrices (here V_ℓ^σ is short hand for an $L \times L$ matrix with a single non-zero element acting on the impurity site equal to V_ℓ^σ defined by (2.8)). The partition function Z then becomes

$$Z = \text{Tr}_{\{\phi_\ell\}} \prod_{\sigma} \det (I + B_1^\sigma B_2^\sigma \dots B_{L_\tau}^\sigma). \quad (2.14)$$

Finally, let O^σ be $LL_\tau \times LL_\tau$ matrices defined as

$$O^\sigma = \begin{pmatrix} I & & & & & B_{L_\tau}^\sigma \\ -B_1^\sigma & I & & & & \\ & -B_2^\sigma & I & & & \\ & & \ddots & \ddots & & \\ & & & -B_{L_\tau-1}^\sigma & I & \end{pmatrix}. \quad (2.15)$$

The final form of the partition function can then be expressed as a product of the determinants of these matrices

$$Z = \text{Tr}_{\{\phi_\ell\}} \det O^\dagger \det O^\downarrow. \quad (2.16)$$

The most important property of these matrices is that their inverse is the imaginary-time green's function

$$g_{ij}^\sigma(\tau_\ell, \tau_{\ell'}) = \langle T \hat{c}_i(\tau_\ell) \hat{c}_j^\dagger(\tau_{\ell'}) \rangle \quad (2.17)$$

$$= \{O^\sigma\}_{i\ell, j\ell'}^{-1}. \quad (2.18)$$

This can perhaps most easily be seen by considering the partition function in terms of path integrals. Since the Hamiltonian is quadratic in the fermion operators, it is possible to write Z in terms of a Gaussian path integral over Grassman numbers

$$Z = \text{Tr}_{\{\phi_\ell\}} \int \mathcal{D}[\psi^\dagger, \psi] \exp \left\{ \int_0^\beta \psi^\dagger g^{-1} \psi d\tau \right\} \quad (2.19)$$

$$= \text{Tr}_{\{\phi_\ell\}} \det g_\uparrow^{-1} \det g_\downarrow^{-1} \quad (2.20)$$

since the spin sectors are still independent. We can thus identify $g^{-1} = O$, although there are subtleties in the discretization procedure [50]. This equality can be shown directly in the Hamiltonian formalism as well, though the derivation is lengthy (see for instance [49]). In terms of the B matrices defined

Substituting back in g , we find

$$\begin{aligned} e^{V'} g' &= e^V g - e^V g (e^{-V'} - e^{-V}) e^{V'} g' \\ g' &= g + g' - e^{V'-V} g' - g (I - e^{V'-V}) g' \\ &= g + (g - I) (e^{V'-V} - I) g'. \end{aligned} \quad (2.27)$$

Alternatively, we can start with the transpose of O . Carrying through similar steps and transposing back at the end, another Dyson equation can be derived

$$g' = g + (g' - I) (I - e^{V-V'}) g. \quad (2.28)$$

The Dyson equations (2.27) and (2.28) are the primary tools of the Hirsch-Fye impurity algorithm. In order to calculate expectation values of observables, we need to trace over all auxiliary spin configurations. If we can find one such green's function, we can use these to generate all the others. In their current form, however, g and O are $LL_\tau \times LL_\tau$ matrices which are cumbersome to perform practical computation with. However, the simple form of the effective potential V that acts only on the impurity site allows for a major simplification

$$\begin{aligned} g_{dd} &= g_{dd} + \sum_{i,j} (g - I)_{di} (e^{V'-V} - I)_{ij} g'_{jd} \\ &= g_{dd} + \sum_{i,j} (g - I)_{di} (e^{V'-V} - I) \delta_{ij} \delta_{id} g'_{jd} \\ &= g_{dd} + (g_{dd} - I) (e^{V'-V} - I) g'_{dd}. \end{aligned} \quad (2.29)$$

Solving this equation for g'_{dd}

$$g'_{dd} = A_{dd}^{-1} g_{dd}, \quad A_{dd} = I - (g_{dd} - I) (e^{V'-V} - I). \quad (2.30)$$

We can now update the $L_\tau \times L_\tau$ imaginary-time impurity green's function without keeping track of any details of the environment. We will see that we can in fact perform the whole calculation keeping only g_{dd} .

2.1.3 The Monte Carlo Algorithm

By formally setting all the auxiliary spin variables to zero $\phi_\ell = 0$, we can turn off the interaction, leaving us with the non-interacting Anderson model. Since the green's function can be solved for by taking matrix elements of¹

$$(\partial_\tau + H_0) g^0 = I, \quad (2.31)$$

¹See Hewson, §1.2 and §5.2 [12].

this provides a means of calculating an initial green's function, from which we can calculate the interacting green's function for any spin configuration via the Dyson equation (2.27). The exact form of g_{dd}^0 will be discussed later.

The full, interacting green's function can be calculated as

$$\langle g \rangle = \frac{\text{Tr}_{\{\phi_\ell\}} g \det O^\uparrow \det O^\downarrow}{\text{Tr}_{\{\phi_\ell\}} \det O^\uparrow \det O^\downarrow}, \quad (2.32)$$

but summing over the whole auxiliary spin space is impossible for large L_τ . Instead the sum is estimated using a Metropolis-like Monte Carlo algorithm

$$\langle g \rangle = \sum_{\{\phi_\ell\}} P(\{\phi_\ell\}) g, \quad P(\{\phi_\ell\}) = \frac{\det O^\uparrow \det O^\downarrow}{Z}. \quad (2.33)$$

The distribution P is generated using a Markov chain where the probability of flipping a single spin $\phi_s \rightarrow \phi'_s = -\phi_s$ is

$$R \equiv P(\phi_s \rightarrow \phi'_s) = \frac{\det O'^\uparrow \det O'^\downarrow}{\det O^\uparrow \det O^\downarrow}. \quad (2.34)$$

The ratio R can be evaluated with the help of the Dyson equation (2.27) for the entire matrix g

$$\begin{aligned} R &= \frac{\det O'^\uparrow \det O'^\downarrow}{\det O^\uparrow \det O^\downarrow} = \frac{\det g^\uparrow \det g^\downarrow}{\det g'^\uparrow \det g'^\downarrow} = \frac{\det A^\uparrow g'^\uparrow \det A^\downarrow g'^\downarrow}{\det g'^\uparrow \det g'^\downarrow} \\ &= \det A^\uparrow \det A^\downarrow, \end{aligned} \quad (2.35)$$

with $A^\sigma = I - (g^\sigma - I)(e^{V'^\sigma - V^\sigma} - I)$. Dropping the spin index σ , for a single auxiliary spin flip the matrix $(e^{V' - V} - I)$ has a single non-zero element. Thus the matrix A has a simple form and the determinant can easily be evaluated. The matrix elements of A are (here i, j, k are spatial indices and ℓ, ℓ', ℓ'' are temporal indices)

$$\begin{aligned} A_{i\ell, j\ell'} &= \delta_{ij} \delta_{\ell\ell'} + \sum_{k\ell''} (g_{ik}(\tau_\ell, \tau_{\ell''}) - \delta_{ik} \delta_{\ell\ell''}) (e^{V' - V} - I)_{k\ell'', j\ell'} \\ &= \delta_{ij} \delta_{\ell\ell'} + (g_{id}(\tau_\ell, \tau_s) - \delta_{id} \delta_{\ell s}) (e^{V'_s - V_s} - 1). \end{aligned} \quad (2.36)$$

The matrix has non-zero elements along the diagonal and in one column

$$A = \begin{pmatrix} 1 & & & A_{11,ds} & & \\ & 1 & & A_{12,ds} & & \\ & & \ddots & \vdots & & \\ & & & A_{ds,ds} & & \\ & & & \vdots & & \\ & & & A_{LL\tau,ds} & & 1 \end{pmatrix}. \quad (2.37)$$

The determinant can easily be evaluated by expanding along the ds 'th row

$$R = \det A = A_{ds,ds} = 1 + (g_{dd}(\tau_s, \tau_s) - 1)(e^{V'_s - V_s} - 1). \quad (2.38)$$

This ratio again depends only on the impurity green's function g_{dd} . We can thus perform Monte Carlo sampling of the auxiliary spin field configurations keeping track only of the impurity green's function. In general this ratio is a complex number, and for certain models the algorithm suffers from the sign-problem. As discussed in further detail below, however, so long as there is only one impurity site at which interactions are included, this ratio is positive definite and thus suitable for use as a probability.

A_{dd}^{-1} (see Eq. (2.30)) also has a particularly simple form for single flips,

$$A_{dd}^{-1} = \begin{pmatrix} 1 & & & -\frac{A_{d1,ds}}{A_{ds,ds}} & & \\ & 1 & & -\frac{A_{d2,ds}}{A_{ds,ds}} & & \\ & & \ddots & \vdots & & \\ & & & A_{ds,ds}^{-1} & & \\ & & & \vdots & & \\ & & & -\frac{A_{dL\tau,ds}}{A_{ds,ds}} & & 1 \end{pmatrix}. \quad (2.39)$$

As a consequence, the matrix product $g'_{dd} = A_{dd}^{-1} g_{dd}$ can be performed in $O(L_\tau^2)$ steps instead of the $O(L_\tau^3)$ steps required to numerically invert A_{dd}

$$g'_{dd}(\tau_\ell, \tau_{\ell'}) = g_{dd}(\tau_\ell, \tau_{\ell'}) + (g_{dd}(\tau_\ell, \tau_s) - \delta_{\ell s}) T_s g_{dd}(\tau_s, \tau_{\ell'}), \quad (2.40)$$

$$T_s = \frac{e^{V'_s - V_s} - 1}{1 + (1 - g_{dd}(\tau_s, \tau_s))(e^{V'_s - V_s} - 1)}. \quad (2.41)$$

We are now in a position to describe the algorithm.

1. Calculate g_{dd}^0 for the appropriate non-interacting Anderson model from Eq. (2.31).

2. Pick an initial spin configuration $\{\phi_\ell\}$ and calculate g_{dd} via

$$g_{dd} = [A_{dd}^0]^{-1} g_{dd}^0, \quad A_{dd}^0 = I - (g_{dd}^0 - I)(e^V - I). \quad (2.42)$$

The matrix A_{dd}^0 does not have the simple form (2.37) so the inverse must be calculated numerically.

3. Perform Metropolis spin flips with probability $P(\phi_s \rightarrow \phi'_s)$ given by Eqs. (2.34) and (2.35). Update g_{dd} after each flip using Eq. (2.40). These single-flip updates require only $O(L_\tau^2)$ operations.
4. At regular intervals check for numerical drift using $A_{dd}^0 g_{dd} = g_{dd}^0$. If required, recalculate g_{dd} using Eq. (2.42). The Hirsch-Fye algorithm is in general very stable numerically (much more so than the BSS algorithm that relies on evaluating matrix products such as Eq. (2.21) [49]). As a result the $O(L_\tau^3)$ matrix inversion rarely needs to be performed.

It must be emphasized again that the significant simplification of using only g_{dd} rather than the entire matrix g (or equivalently O) is possible due to the simple form of the interaction term. Related algorithms developed for studying the Hubbard model either keep track only of spatial correlations (leading to $L \times L$ matrices), or keep track of all spatial and temporal correlations. Note as well that with the exception of the initial calculation of g_{dd}^0 , the algorithm needs no further input from the specific form of \hat{H}_0 .

2.2 Observables and Wick's Theorem

The algorithm naturally gives us access to the imaginary time impurity green's function. Due to the quadratic form of the Hamiltonian at each spin configuration, four-point (and higher) green's functions can also be calculated via Wick's theorem, which follows in the standard fashion by differentiating Eq. (2.19). For instance, the local moment of the impurity can expressed

$$\begin{aligned} \langle \hat{\sigma}_z^2 \rangle &= \langle (\hat{n}_{d\uparrow} - \hat{n}_{d\downarrow})^2 \rangle \\ &= \langle \hat{n}_{d\uparrow}^2 \rangle - 2\langle \hat{n}_{d\uparrow} \hat{n}_{d\downarrow} \rangle + \langle \hat{n}_{d\downarrow}^2 \rangle \\ &= \langle \hat{d}_\uparrow^\dagger \hat{d}_\uparrow \hat{d}_\uparrow^\dagger \hat{d}_\uparrow \rangle + \dots \end{aligned} \quad (2.43)$$

Applying Wick's theorem to this first term,

$$\langle \hat{d}_\uparrow^\dagger \hat{d}_\uparrow \hat{d}_\uparrow^\dagger \hat{d}_\uparrow \rangle = \langle \hat{d}_\uparrow^\dagger \hat{d}_\uparrow \rangle \langle \hat{d}_\uparrow^\dagger \hat{d}_\uparrow \rangle + \langle \hat{d}_\uparrow^\dagger \hat{d}_\uparrow \rangle \langle \hat{d}_\uparrow \hat{d}_\uparrow^\dagger \rangle, \quad (2.44)$$

and the third contraction vanishes. The impurity site's contribution to the magnetic susceptibility can be calculated similarly.

Unfortunately, the cost of throwing away the conduction electron green's functions is that we no longer have access to global properties of the system. For instance, the free energy $\langle H \rangle - \mu \langle N \rangle$ would require the entire matrix g to be kept, not just g_{dd} . This is in principle possible, but computationally extremely challenging. With some work, however, we can calculate some local properties of a finite number of conduction electrons (and their correlations), at the cost of keeping another $L_\tau \times L_\tau$ matrix at each step of the Monte Carlo for each green's function needed. This will be described in further detail in Chap. 3.

2.3 The Fermion Sign Problem

As mentioned above, the ratio R given by Eq. (2.35) is in general a complex number. It is simply shown that particle-hole symmetry, of the type

$$\begin{aligned} \hat{c}_{d\uparrow}^\dagger &\rightarrow \hat{c}_{d\downarrow} & \hat{c}_{d\uparrow} &\rightarrow \hat{c}_{d\downarrow}^\dagger \\ \hat{c}_{k\uparrow}^\dagger &\rightarrow -\hat{c}_{k\downarrow} & \hat{c}_{k\uparrow} &\rightarrow -\hat{c}_{k\downarrow}^\dagger, \quad \text{etc.} \end{aligned} \quad (2.45)$$

implies that the ratio R is real and non-negative. Under the above symmetry transformation,

$$\begin{aligned} \hat{V}_\ell^\sigma &= \lambda\sigma\phi_\ell \hat{c}_{d\sigma}^\dagger \hat{c}_{d\sigma} \rightarrow \lambda\sigma\phi_\ell \hat{c}_{d\sigma'} \hat{c}_{d\sigma'}^\dagger \\ &= \lambda\sigma\phi_\ell (1 - \hat{n}_{d\sigma'}) \\ &= \lambda\sigma\phi_\ell + \hat{V}_\ell^{\sigma'}. \end{aligned} \quad (2.46)$$

The determinant of O^σ can be written in terms of the original trace over fermion degrees of freedom

$$\det O^\sigma = \text{Tr} \prod_{\ell=1}^{L_\tau} e^{-\Delta\tau \hat{H}_0} e^{\hat{V}_\ell^{\sigma'}} e^{\lambda\sigma\phi_\ell} = \prod_{\ell=1}^{L_\tau} e^{\lambda\sigma\phi_\ell} \det O^{\sigma'}, \quad (2.47)$$

and since the matrix O^σ contains only real elements, the ratio

$$R = \frac{\det O'^\uparrow \det O'^\downarrow}{\det O^\uparrow \det O^\downarrow} = \frac{\prod_{\ell=1}^{L_\tau} e^{\lambda\phi'_\ell} (\det O'^\uparrow)^2}{\prod_{\ell=1}^{L_\tau} e^{\lambda\sigma\phi_\ell} (\det O^\uparrow)^2} \quad (2.48)$$

is real and non-negative.

However, it has recently been shown by Yoo *et al.* [54] that, provided the Hamiltonian can be transformed into a one-dimensional problem, the ratios of the determinants $\det O^\sigma$ are individually positive semi-definite. So long as there is only a single Anderson impurity, this can be done even away from the

particle-hole symmetric point ($\epsilon_d = -U/2$) and when an Aharonov-Bohm flux is applied.

2.4 Complexity

Because performing a full update of g_{dd} requires a matrix inversion, the algorithm scales as $O(L_\tau^3)$ making the $T \rightarrow 0$ limit computationally demanding. There is no direct dependence on L , the size of the system to be studied except possibly in the calculation of g_{dd}^0 ; indeed the initial study on the Anderson model was conducted in the thermodynamic limit at which g_{dd}^0 can be calculated exactly.

The persistent current is of order $1/L$, however, which makes stochastic estimation of j more difficult as L increases. This limit has not yet been tested empirically, but we hope that useful calculations can be performed at significantly larger system sizes than have currently been investigated.

Chapter 3

Persistent Current Through Non-Interacting Quantum Dots

The Hirsch-Fye algorithm provides a numerical estimate of the impurity's imaginary-time green's function. While in principle all correlation functions are available to the algorithm, only a small, finite number can in practise be obtained for large system sizes due to the computational effort required. As mentioned earlier, the consequence is that the ground state or free energy cannot be directly calculated. Instead, the equilibrium persistent current can be calculated from a small number of correlation functions, as will be described below.

In this chapter I present calculations of the persistent current in rings coupled to a non-interacting impurity in the two geometries discussed in Sec. 1.5 (embedded and side coupled dots). The calculations are performed using the non-interacting imaginary-time green's functions (ITGF) that form the input to the Monte Carlo algorithm described in the previous chapter. In order to check the ITGF results in detail, they are compared to an expansion in powers of $1/L$ of the persistent current through a scattering potential due to Gogolin and Prokof'ev (GP) [55], and to single-particle exact diagonalization (ED) results. Most importantly, this verifies the validity of the ITGF approach and the expressions used for the current that are essential for the QMC algorithm. However, the results presented below also highlight the particularly sensitive physics of persistent currents. Even in non-interacting systems, the persistent current shows a strong dependence on effects of the ring geometry, the parity of the number of sites L and electrons N , and the choice of ensemble averaging (that is, whether the particle number N or the chemical potential μ is held fixed).

The ITGF approach yields finite temperature results with fixed chemical potential μ . In contrast, the GP expansion is a ground state result with fixed particle number N . In some cases these yield essentially identical results for

the current, however in other cases there are significant differences between the current in the different ensembles. All results have been checked in detail against the exact diagonalization results which can be run in either ensemble.

In general all derivations below are outlined for arbitrary hopping strength t , however all numerical results presented in this thesis are for $t = 1$.

3.1 The Current Operator

The time derivative of the charge density operator $\hat{q}_i = -e\hat{c}_i^\dagger\hat{c}_i$ in a tight-binding Hamiltonian with only nearest-neighbour couplings t (see (1.8)) is

$$\begin{aligned}\dot{\hat{q}}_i &= \frac{i}{\hbar}[\hat{H}, \hat{q}_i] \\ &= \frac{-iet}{\hbar} \left[\hat{c}_{i+1}^\dagger\hat{c}_i - \hat{c}_i^\dagger\hat{c}_{i+1} + \hat{c}_{i-1}^\dagger\hat{c}_i - \hat{c}_i^\dagger\hat{c}_{i-1} \right].\end{aligned}\quad (3.1)$$

Using $\nabla \cdot O = O_i - O_{i-1}$ as a lattice derivative, this can be rearranged as a continuity equation for the charge density

$$\dot{\hat{q}} + \nabla \cdot \hat{j} = 0 \quad (3.2)$$

which defines the current operator \hat{j}_i

$$\hat{j}_i = iet \left[\hat{c}_{i+1}^\dagger\hat{c}_i - \hat{c}_i^\dagger\hat{c}_{i+1} \right], \quad (3.3)$$

where we have set $\hbar = (c = k_B =)1$.

We can then write the finite-temperature current in terms of the imaginary-time green's function. As in Chap. 2, define $g_{ij}(\tau_\ell, \tau_{\ell'}) = \langle T \hat{c}_i(\tau_\ell)\hat{c}_j^\dagger(\tau_{\ell'}) \rangle$ (T is the time-ordering operator), so the expression for the current becomes

$$\langle \hat{j}_i \rangle = iet \lim_{\tau \rightarrow 0^-} \left[g_{i+1,i}(\tau, 0) - g_{i,i+1}(\tau, 0) \right]. \quad (3.4)$$

These green's functions can be calculated straightforwardly in the non-interacting Anderson model (for now it is convenient to stay in momentum space)

$$\hat{H}_0 = \sum_{k,\sigma} \epsilon_k \hat{c}_{k\sigma}^\dagger \hat{c}_{k\sigma} + \sum_{k,\sigma} [V_k \hat{c}_{k\sigma}^\dagger \hat{c}_{d\sigma} + \text{H.c.}] + \sum_{\sigma} \epsilon_d \hat{n}_{d\sigma}. \quad (3.5)$$

The tight-binding dispersion relation $\epsilon_k = -2t \cos k$ will hold for both geometries, but the hybridization V_K is geometry dependent. Evaluating matrix elements of the operator equation [12]

$$(\hat{H}_0 - \mu\hat{N} + i\omega_n)g(i\omega_n) = I \quad (3.6)$$

where $\omega_n = (2n + 1)\pi/\beta$ are the fermionic Matsubara frequencies, we get

$$g_{dd}^\sigma(i\omega_n) = \frac{1}{i\omega_n + \epsilon_d - \mu - \sum_k \frac{|V_k|^2}{i\omega_n + \epsilon_k - \mu}} \quad (3.7)$$

$$g_{dk}^\sigma(i\omega_n) = -\frac{V_k^*}{i\omega_n + \epsilon_k - \mu} g_{dd}^\sigma(i\omega_n) \quad (3.8)$$

$$g_{kd}^\sigma(i\omega_n) = -\frac{V_k}{i\omega_n + \epsilon_k - \mu} g_{dd}^\sigma(i\omega_n) \quad (3.9)$$

$$g_{kk'}^\sigma(i\omega_n) = \frac{\delta_{kk'}}{i\omega_n + \epsilon_k - \mu} + \frac{V_k}{i\omega_n + \epsilon_k - \mu} g_{dd}^\sigma \frac{V_{k'}^*}{i\omega_n + \epsilon_{k'} - \mu} \quad (3.10)$$

At this point the spin index σ will be dropped since the two spin channels are independent and identical in the non-interacting case. The electron spin will still contribute to parity effects. From these expressions, the spatial correlation functions (and thus the current) can be extracted by inverse Fourier transforming, but since those transformations are different for the two geometries, they will be discussed later. Note that where one takes the complex conjugate of the hybridization depends on the definition of the hybridization: here $\langle k|H|d\rangle = V_k$, which is opposite of the definition used in Hewson [12].

3.2 Embedded Quantum Dot

3.2.1 Imaginary-Time Green's Function (ITGF) Approach

The embedded quantum dot can be modelled by the following tight-binding Hamiltonian

$$\begin{aligned} \hat{H}_{\text{EQD}} = & -t \sum_{\substack{j=1 \\ \sigma}}^{L-2} \left[\hat{c}_{j\sigma}^\dagger \hat{c}_{j+1\sigma} + \hat{c}_{j+1\sigma}^\dagger \hat{c}_{j\sigma} \right] + \epsilon_d \sum_{\sigma} \hat{n}_{d\sigma} + U \hat{n}_{d\uparrow} \hat{n}_{d\downarrow} \\ & - t' \left[\hat{c}_{d\sigma}^\dagger (e^{i\alpha/2} \hat{c}_{1\sigma} + e^{-i\alpha/2} \hat{c}_{L-1\sigma}) + \text{H.c.} \right]. \end{aligned} \quad (3.11)$$

The effects of the Aharonov-Bohm flux Φ are included by adding a total phase twist of $\alpha = 2\pi\Phi/\Phi_0$ in the bonds between the impurity and the two sites that couple directly to it. Fourier-transforming to obtain the original momentum-space Hamiltonian (3.5),

$$\hat{c}_j = \sqrt{\frac{2}{L}} \sum_k \sin(kj) \hat{c}_k, \quad k = \frac{\pi n}{L}, \quad n = 1 \dots L-1 \quad (3.12)$$

gives the standard dispersion relation $\epsilon_k = -2t \cos k$ and the hybridization

$$V_k = -t' \sqrt{\frac{2}{L}} (e^{i\alpha/2} \sin k + e^{-i\alpha/2} \sin k(L-1)). \quad (3.13)$$

The effects of the flux are encoded entirely in this expression for the hybridization.

We are interested in the correlations between adjacent sites on the ring. By inverse Fourier-transforming Eqs. (3.7), these spatial correlations can be found

$$\begin{aligned} g_{dj}(\tau_\ell, \tau_{\ell'}) &= \langle \text{T} \hat{c}_d(\tau_\ell) \hat{c}_j^\dagger(\tau_{\ell'}) \rangle \\ &= \sqrt{\frac{2}{L}} \sum_k \sin kj \left[\frac{1}{\beta} \sum_{\omega_n} e^{-i\omega_n(\tau_\ell - \tau_{\ell'})} g_{dk}(i\omega_n) \right] \\ g_{dj}(i\omega_n) &= \sqrt{\frac{2}{L}} \sum_k \frac{V_k^* \sin kj}{i\omega_n + \epsilon_k} g_{dd}(i\omega_n), \end{aligned} \quad (3.14)$$

and similarly

$$g_{jd}(i\omega_n) = \sqrt{\frac{2}{L}} \sum_k \frac{V_k \sin kj}{i\omega_n + \epsilon_k} g_{dd}(i\omega_n) \quad (3.15)$$

$$g_{jj'}(i\omega_n) = \frac{2}{L} \left[\sum_k \frac{\sin kj \sin kj'}{i\omega_n + \epsilon_k} + \sum_{kk'} \frac{V_k \sin kj}{i\omega_n + \epsilon_k} g_{dd}(i\omega_n) \frac{V_{k'}^* \sin k'j'}{i\omega_n + \epsilon_{k'}} \right], \quad (3.16)$$

although strictly we need here only the green's functions g_{d1} and g_{1d} . We can now calculate the persistent current by Fourier-transforming back to the imaginary time domain; for instance¹

$$g_{dd}(\tau_\ell - \tau_{\ell'}) = \frac{1}{\beta} \sum_{\omega_n} e^{i\omega_n(\tau_\ell - \tau_{\ell'})} g_{dd}(i\omega_n). \quad (3.17)$$

We can now calculate the current. However, since the hopping between the impurity site and the adjacent site is modified by the effects of the flux, the definition of current operator between these links changes:

$$\frac{jL}{e v_F} = \frac{Lt'}{t} \text{Im} \left(e^{i\alpha/2} g_{10}(0^-, 0) - e^{-i\alpha/2} g_{01}(0^-, 0) \right). \quad (3.18)$$

¹There is a discontinuity in these green's functions at equal times, stemming from the fermionic anti-commutation relations: $\lim_{\delta \rightarrow 0^+} \langle \text{T} c_i(\tau_\ell) c_j^\dagger(\tau_\ell + \delta) \rangle + \langle \text{T} c_i(\tau_\ell) c_j^\dagger(\tau_\ell - \delta) \rangle = \delta_{ij}$. The Fourier transform (3.17) will give the midpoint, so one must pick either limit by adding or subtracting $\delta_{ij}/2$.

3.2.2 Gogolin and Prokof'ev (GP) Approach

Gogolin and Prokof'ev expressed the persistent current in a ring containing a potential scattering centre in terms of its transmission coefficient [55]. Expanding in powers of $1/L$, they found that the persistent current to $O(1/L)$ depends only on the parity of the number of electrons in each spin channel and the transmission coefficient $T(k_F)$ at the Fermi level of the system with no applied flux. The current contributed by each spin channel is given by

$$\frac{jL}{eV_F} = \begin{cases} -\frac{\sqrt{T(k_F)} \sin \alpha \left[\arccos \left(\sqrt{T(k_F)} \cos \alpha \right) + \pi \right]}{\pi \sqrt{1 - T(k_F) \cos^2 \alpha}} & \text{if } N_\sigma \text{ even,} \\ -\frac{\sqrt{T(k_F)} \sin \alpha \left[\arccos \left(\sqrt{T(k_F)} \cos \alpha \right) \right]}{\pi \sqrt{1 - T(k_F) \cos^2 \alpha}} & \text{if } N_\sigma \text{ odd.} \end{cases} \quad (3.19)$$

where N_σ refers to the number of electrons in that spin channel. The total current is the sum of contributions from each spin channel, thus when both spin channels have either even or odd occupancies (N even), the current is 2π periodic. When one spin channel has even occupancy and the other has odd (N odd), the periodicity halves to π . This result is valid at $T = 0$ with fixed particle number.

In order to calculate the transmission coefficient of the non-interacting dot, we can substitute a one-dimensional scattering ansatz $\psi_{j<0} = e^{ikj} + \rho e^{-ikj}$, $\phi_{j>0} = \tau e^{ikj}$ and dispersion relation $\epsilon_k = -2t \cos k$ into the lattice Schrodinger equation

$$\epsilon_k \phi_{|j|>1} = -t(\phi_{j+1} + \phi_{j-1}) \quad (3.20a)$$

$$\epsilon_k \phi_{\pm 1} = -t\phi_{\pm 2} - t' \phi_d \quad (3.20b)$$

$$\epsilon_k \phi_d = -t'(\phi_1 + \phi_{-1}) + \epsilon_d \phi_d \quad (3.20c)$$

Solving for $T(k) = |\tau|^2$, this yields

$$T(k) = \left[1 + \frac{t^2}{4t'^4 \sin^2 k} \left[\epsilon_k \left(1 - \frac{t'^2}{t^2} \right) - \epsilon_d \right] \right]^{-1}. \quad (3.21)$$

At $\epsilon_F = 0$ this reduces to

$$T(k_F) = \frac{4t'^4}{4t'^4 + t^2 \epsilon_d^2}. \quad (3.22)$$

The current for a non-interacting EQD is then given by Eqs. (3.19) and (3.22). These expressions reduce to those of a non-interacting ideal ring (1.10) in the

limit that $t' \rightarrow t$ and $\epsilon_d \rightarrow 0$, upon which the Hamiltonian (3.11) reduces to that of an ideal tight-binding ring.

3.2.3 Single-particle Exact Diagonalization (ED) Approach

When U is zero, the $L \times L$ matrix h_0 (see Eq. (2.9)) corresponding to the non-interacting Hamiltonian can be diagonalized to find the single-particle energies ϵ_ν and eigenstates $|\nu\rangle$ of the system. The current can then be evaluated

$$\langle \hat{j} \rangle = \text{Tr } \rho \hat{j} \quad (3.23)$$

in the basis of the eigenstates. The density matrix ρ can be calculated in either the finite-temperature grand-canonical ensemble using the Fermi-Dirac distribution $\rho_{\nu\nu} = (e^{\beta(\epsilon_\nu - \mu)} + 1)^{-1}$, or in the ground state canonical ensemble by filling up the lowest energy states with N electrons. The particle number can also be easily evaluated

$$\langle \hat{N} \rangle = \text{Tr } \rho \hat{N}, \quad (3.24)$$

which will be useful in understanding the differences between the canonical and grand-canonical results. Since we have only focused on the correlations between a few sites, we cannot obtain the total particle number from the ITGF approach. This method gives identical results to the ITGFs at finite T but despite its relative simplicity, it cannot provide the input required by the Hirsch-Fye QMC algorithm.

3.3 Side Coupled Quantum Dot

3.3.1 ITGF Approach

We begin with the tight-binding, Anderson impurity model of an L -site ring side-coupled to a quantum dot

$$\begin{aligned} \hat{H}_{SCQD} = & -t \sum_{\substack{j=0 \\ \sigma}}^{L-2} \left[\hat{c}_{j\sigma}^\dagger \hat{c}_{j+1\sigma} + \hat{c}_{j+1\sigma}^\dagger \hat{c}_{j\sigma} \right] - t' \sum_{\sigma} \left[\hat{c}_{0\sigma}^\dagger \hat{c}_{d\sigma} + \hat{c}_{d\sigma}^\dagger \hat{c}_{0\sigma} \right] \\ & + \epsilon_d \sum_{\sigma} \hat{n}_{d\sigma} + U \hat{n}_{d\uparrow} \hat{n}_{d\downarrow}. \end{aligned} \quad (3.25)$$

The effects of the flux α are included in this geometry by gauge-transforming

them into the boundary conditions for the ring states

$$\hat{c}_j = e^{i\alpha} \hat{c}_{j+L}. \quad (3.26)$$

We can recover the momentum-space Hamiltonian (3.5) by setting

$$\hat{c}_j = \frac{1}{\sqrt{L}} \sum_k e^{ikj} \hat{c}_k, \quad k_n = \frac{2\pi n}{L} + \frac{\alpha}{L}, \quad n = 1, 2, \dots, L. \quad (3.27)$$

This gives the usual dispersion relation and the hybridization $V_k = -t'/\sqrt{L}$. The effects of the flux are encoded entirely in the choice of wave vectors.

The relevant green's functions for the persistent current are the correlations between sites 0 and 1 on the ring itself (or any other two adjacent sites). They are given by

$$g_{dj}(i\omega_n) = \frac{1}{\sqrt{L}} \sum_k \frac{V_k^* e^{-ikj}}{i\omega_n + \epsilon_k} g_{dd}(i\omega_n) \quad (3.28)$$

$$g_{jd}(i\omega_n) = \frac{1}{\sqrt{L}} \sum_k \frac{V_k e^{ikj}}{i\omega_n + \epsilon_k} g_{dd}(i\omega_n) \quad (3.29)$$

$$g_{jj'}(i\omega_n) = \frac{1}{L} \left[\sum_k \frac{e^{ik(j-j')}}{i\omega_n + \epsilon_k} + \sum_{kk'} \frac{V_k e^{ikj}}{i\omega_n + \epsilon_k} g_{dd}(i\omega_n) \frac{V_{k'}^* e^{-ik'j'}}{i\omega_n + \epsilon_{k'}} \right] \quad (3.30)$$

As in the EQD case, we can now transform back to the imaginary time domain and calculate the current

$$\frac{jL}{ev_f} = L \text{Im} \left(g_{10}(0^-, 0) - g_{01}(0^-, 0) \right). \quad (3.31)$$

3.3.2 GP Approach

Again we can compare to the GP expansion based on the transmission coefficient of the side-coupled dot. It is important to emphasize the difference in this geometry between L (the number of sites in the ring only) and N , the total number of electrons. At half-filling, the impurity contributes an electron as well, hence $N = L + 1$.

Starting with the scattering ansatz $\psi_{j<0} = e^{ikj} + \rho e^{-ikj}$, $\phi_{j>0} = \tau e^{ikj}$, the transmission coefficient of the side-coupled quantum dot can be found using the single-particle lattice Schrodinger equation

$$\epsilon_k \phi_{j \neq 0} = -t(\phi_{j+1} + \phi_{j-1}) \quad (3.32a)$$

$$\epsilon_k \phi_0 = -t(\phi_1 + \phi_{-1}) - t' \phi_d \quad (3.32b)$$

$$\epsilon_k \phi_d = -t' \phi_0 + \epsilon_d \phi_d. \quad (3.32c)$$

Substituting in the scattering ansatz and tight-binding dispersion relation, the transmission coefficient $T = |\tau|^2$ for each spin channel is

$$T(k) = \left(1 + \frac{t'^4}{4t^2 \sin^2 k (\epsilon_k - \epsilon_d)^2}\right)^{-1}, \quad (3.33)$$

which becomes

$$T(k_f) = \frac{\epsilon_d^2}{\epsilon_d^2 + t'^4/4t^2} \quad (3.34)$$

when $\epsilon_F = 0$. The current is then given by Eqs. (3.34) and (3.19). Notably, this formula predicts that at the particle-hole symmetric point ($\epsilon_d = 0$) there will be no transmission and thus no persistent current. When the impurity is decoupled from the ring ($t' = 0$), the current becomes that of an ideal ring, though subtleties of counting electrons remain.

3.3.3 ED Approach

The single-particle exact diagonalization is done in the same way as described for the EQD geometry. The single-particle SCQD Hamiltonian is $L + 1 \times L + 1$ due to the side-coupled impurity. The current and particle number are calculated as before.

3.4 Results

3.4.1 Finite Temperature Effects

In general, the persistent current is suppressed by a finite temperature. Considering first the case of an ideal ring (with L even), the effects of temperature are shown in Fig. 3.1(b). The typical energy spacing between near the Fermi level is of the order of

$$\Delta\epsilon \approx -2t \sin \frac{\pi}{L}. \quad (3.35)$$

However, the relevant gap is between the highest right- and left-moving states (see Fig. 3.1(a)) whose degeneracy is broken by a finite applied flux. This spacing is of the order of $[\alpha]$. This emphasizes the importance of the points $[\alpha] = 0$ where levels cross. Near the $T = 0$ discontinuities where level occupancies change, the gap is vanishingly small. This makes such discontinuities difficult to resolve at finite temperature. The finite temperature current far away from these points should converge on the ground state current at higher temperatures than near the discontinuities. This feature is characteristic of the temperature dependence of the current in more realistic rings as higher

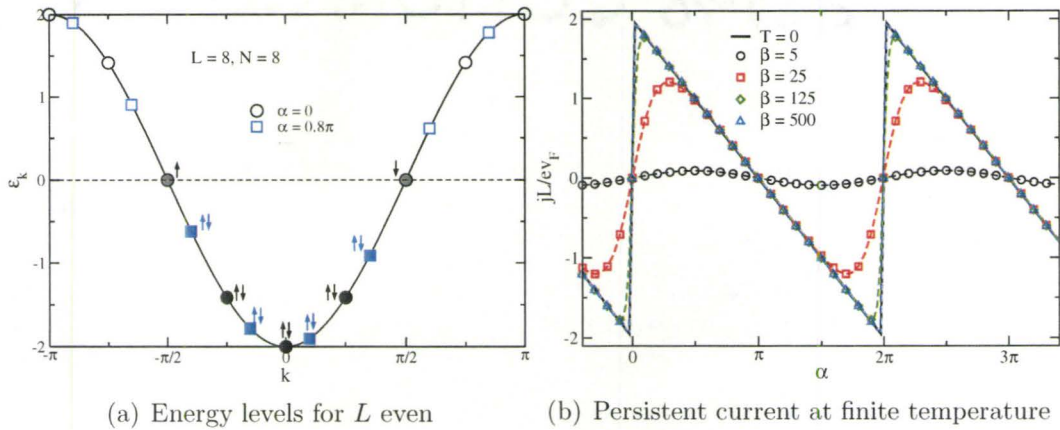


Figure 3.1: (a) Energy levels for an ideal ring with an even number of sites for two values of the flux α . The wave vectors k_n shift to the right as the flux increases. The ground state is degenerate at $\alpha = 0$, but the degeneracy is lifted by a finite applied flux. The splitting is of order $[\alpha]$. The occupied states for fixed particle number N are indicated by the arrows, whereas the occupied states for fixed chemical potential μ are indicated by the filled symbols. In this case the current is identical in the two ensembles. (b) The current at finite temperature. The solid black line is the $T = 0$ GP result. The open symbols are the current calculated at finite temperature using ITGFs. The dashed lines are finite temperature ED results. For $\beta = 500$ the GP and ITGF results are indistinguishable, but at higher temperatures higher harmonics of the current are washed out.

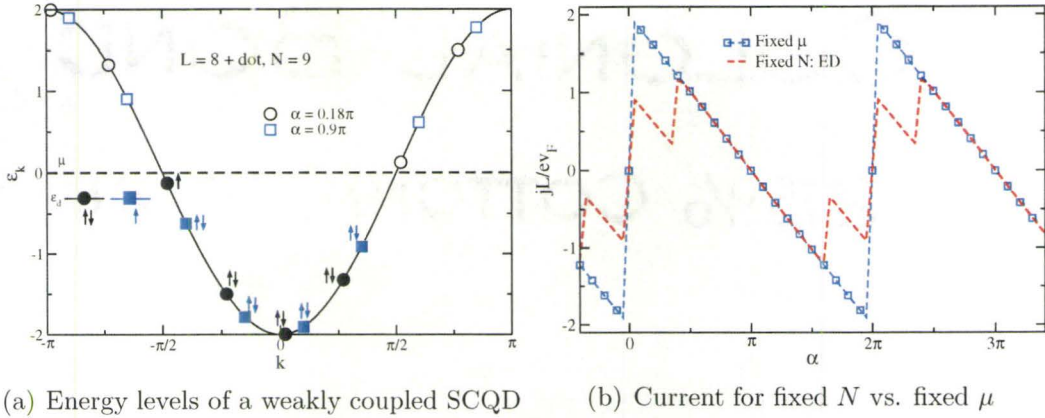


Figure 3.3: (a) Energy levels for an 8-site ring with a weakly coupled impurity at two values of the flux α . When the chemical potential μ is fixed, the impurity occupancy is independent of α (as indicated by the filled symbols). In this case the presence of the impurity is irrelevant to the persistent current. When the particle number N is fixed and the impurity level lies close to the Fermi level, electrons can move between the impurity and ring states as a function of the flux (electron occupation is indicated by the arrows), leading to discontinuities in the current at $T = 0$ not present in the grand-canonical ensemble. (b) Corresponding current calculated by ITGFs (fixed μ) and ED (fixed N) showing the discontinuity in the fixed N current near $\alpha = \pi/2$.

the current, and the site will either be doubly occupied or empty, regardless of the flux α . However, when the impurity energy is close to the Fermi level, the impurity and ring states will mix more strongly (as suggested by the dip in the current predicted by the GP result (3.3)).

We see here the first small difference between fixing the chemical potential and the fixing the particle number. When t' is vanishingly small, the impurity is essentially decoupled from the (now ideal) ring. If the chemical potential is fixed, the occupancy of the site will simply be given by the Fermi-Dirac distribution and not affect the persistent current in any way. Note however, that at $T = 0$ for $\mu = 0$ in this case, $\langle N \rangle = L$ or $L + 2$ depending on whether ϵ_d lies above or below the chemical potential, which does not correspond to half-filling in the fixed-particle case. When N is fixed, the impurity can act as a sort of particle reservoir, leading to discontinuities in the current as the highest occupied levels in the ring cross the impurity site energy (see Fig. 3.3(b)). These discontinuities are not present in the grand-canonical ensemble. These subtle issues of particle counting are less apparent in the symmetric Anderson or Kondo models in which particle-hole symmetry enforces $N = L + 1$ in the SCQD geometry.

When the site is coupled to the ring, the dot suppresses transmission at

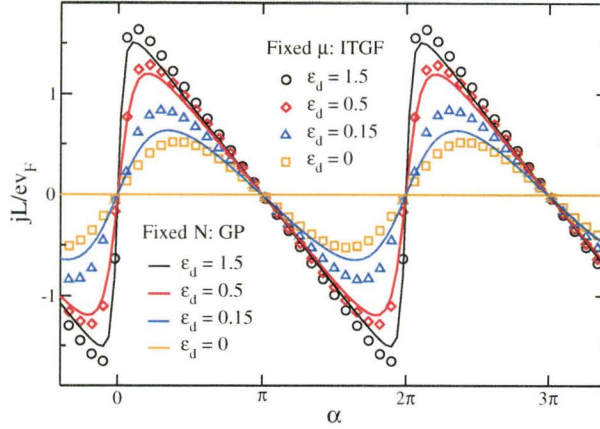


Figure 3.4: Persistent current of a 16 site ring side-coupled to a quantum dot with $t' = 0.6$. When ϵ_d is far from the Fermi level, the transmission through the coupled dot is strong and the current remains nearly ideal. In this regime there is reasonably good agreement between the predictions of the canonical and grand-canonical ensembles. However, as $\epsilon_d \rightarrow \epsilon_F$, the transmission is suppressed (with characteristic width of $t'^2/2t$). In this regime the GP and ITGF results are strikingly different. The GP results predict that the current will be completely suppressed at ϵ_d but the ITGF results show a finite current. See text for discussion.

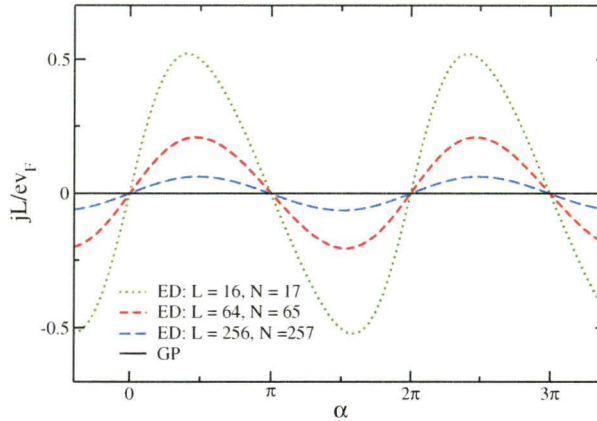


Figure 3.5: Persistent current in the SCQD geometry in the canonical ensemble with $t' = 0.6$ and $\epsilon_d = 0$. The $1/L$ term in the GP expansion predicts a complete suppression of the current. ED results with fixed N show a finite current that decays as the system size increases, indicating the presence of a large $1/L^2$ or higher order term in the GP expansion.

the Fermi level when ϵ_d is within a characteristic width $t'^2/2t$ of ϵ_F . Figure 3.4 shows the current plotted versus the flux for four values of ϵ_d as calculated by ITGFs and the GP expansion (ED results not shown). There is a reasonably good agreement between the GP and ITGF results when ϵ_d is far from ϵ_F , and the discrepancy can be accounted for by the difference between keeping N fixed versus keeping μ fixed (this is confirmed by ED calculations).

The agreement, however, breaks down seriously as the impurity level approaches the Fermi level. In this case the difference is not solely due to working in a different statistical mechanical ensemble. Figure 3.5 shows the current calculated with fixed N at $\epsilon_d = 0$ by ED as the system size increases. (The GP current is proportional to $1/L$ so jL/ev_F remains constant as L increases.) For small system sizes, the current remains large even in the canonical ensemble. However, as the system size increases, the current decays towards the $O(1/L)$ term of the GP expansion. This suggests the presence of large higher order terms in the GP expansion that have not been taken into account.

3.4.3 L odd and Ensemble Effects

The situation when L is odd is more complicated. Even for an ideal ring, there is a drastic difference between the current in the canonical and grand-canonical ensembles. Consider energy levels of an ideal ring with an odd number of sites, shown in Fig. 3.6(a). When the particle number is fixed, the ground state current is discontinuous at $\alpha = n\pi$ as the highest right- and left- moving states cross. When the chemical potential is fixed, however, the discontinuities occur when the states cross the chemical potential. When L is even, the relevant level crossings occur at the chemical potential, so the discontinuities in the current for fixed N and fixed μ occur at the same values of the flux. However, when L is odd, the levels cross the chemical potential (but not each other) when $\alpha = \pi/2 + n\pi$ leading to strong fluctuations in $\langle N \rangle$ for fixed μ . The result is that the characteristic ‘saw-tooth’ curve is shifted by $\pi/2$ in α between the two ensembles. Figure 3.6(b) shows the current in both cases, and the corresponding particle number $\langle N \rangle$.

EQD Results

When the impurity energy level ϵ_d and the coupling t' are shifted from their ideal values, the energy level structure shifts and electrons begin to reflect off of the impurity, shifting and rounding the discontinuities in the persistent current (see Fig. 3.7). The difference between fixing the particle number and fixing chemical potential becomes more apparent. The ITGF results in the grand-canonical ensemble are shown as open symbols, the GP results as a solid line, and the corresponding ED results are shown as dashed lines. When $\epsilon_d \neq 0$ in the non-interacting Anderson model, particle-hole symmetry is broken and the

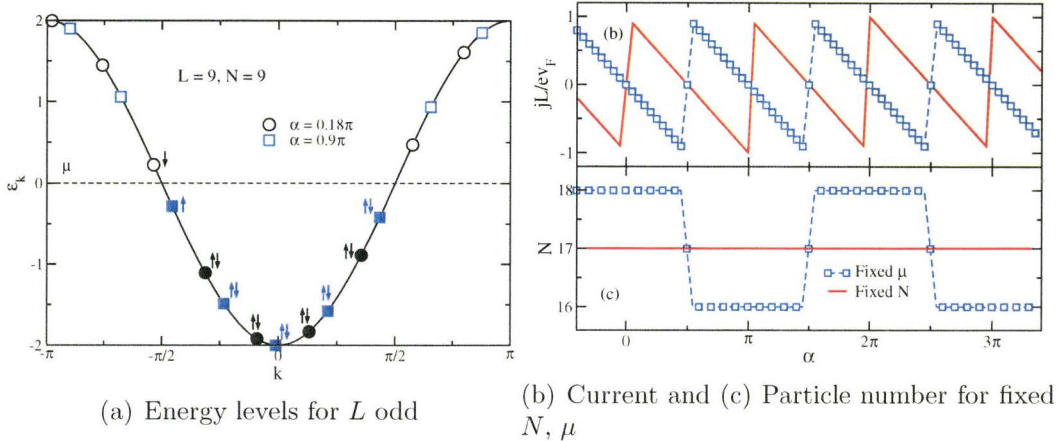


Figure 3.6: (a) Energy levels for an ideal ring with an odd number of sites. In a system with a fixed number of electrons, the highest occupied levels lie above the ‘half-filling’ chemical potential, $\mu = 0$. The degeneracy at $\alpha = 0$ of the right- and left-moving states is broken by a finite applied flux, causing a discontinuity in the occupation number of the highest states at $\alpha = 0$ (occupation numbers for fixed N are indicated by arrows). This level crossing leads to discontinuities in the persistent current at $\alpha = \pi/2$ for fixed N . When μ is fixed at 0, this broken degeneracy does not lead to a change in the occupation number of the right- and left-moving states. The discontinuities occur as the levels cross the chemical potential, when $\alpha = \pi/2 + n\pi$ (occupation numbers for fixed μ are indicated by the filled symbols). (b) The persistent current for fixed N (solid line) jumps at $\alpha = n\pi$. The current for fixed μ (symbols, dashed line) jumps at $\alpha = n\pi + \pi/2$. (c) The corresponding particle number for each ensemble. The total number of electrons for fixed μ jumps by 2 as levels cross the chemical potential.

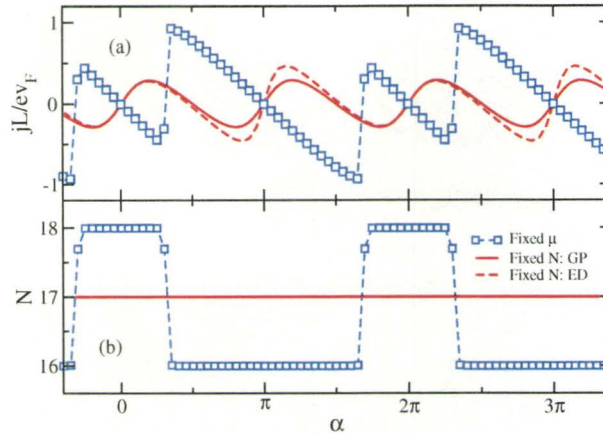


Figure 3.7: Persistent current of a 17 site ring with an embedded dot, $t' = 0.6$, $\epsilon_d = 0.4$. The squares indicate the ITGF result at fixed μ . The solid line indicates the GP result for fixed N . Corresponding ED results are shown as dashed lines. For small system sizes, the π periodicity of the GP expansion is broken in the ED results. This is a result of broken particle-hole symmetry. (b) Corresponding particle numbers. Note the strong fluctuation of the particle number in the fixed μ case that also break the π periodicity in the flux.

π periodicity in the flux is lost (in both ensembles). The loss of π periodicity is not captured, however, by the GP result, suggesting that it is restored as $L \rightarrow \infty$.

SCQD Results

The effects of tuning away from the ideal ring in the SCQD geometry with an odd number of sites are qualitatively similar to those of tuning away from the ideal limit in the EQD case. They are summarized in Fig. 3.8.

3.5 Conclusions

Clearly there are many details that can strongly affect the persistent current, even in non-interacting systems. The effects of finite temperature, choice of statistical-mechanical ensemble, ring geometry, and the parity of both the electron number and the number of sites in the ring have all been discussed in this chapter, and their qualitative effects will remain even when interactions are included. Moreover, it seems likely that all of these effects are relevant to potential experimental situations. In particular, it should be possible to choose an experimental setup such that either the chemical potential or the particle number is fixed.

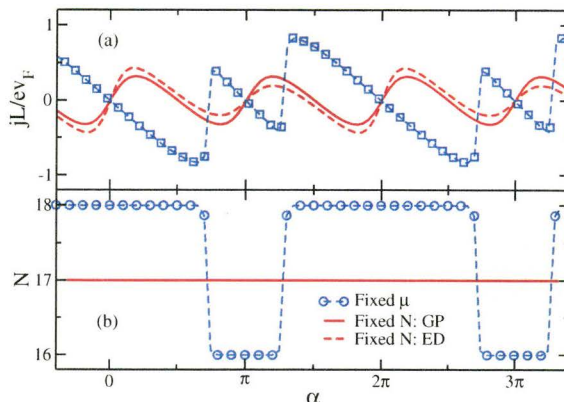


Figure 3.8: (a) Persistent current of a 17-site ring side-coupled to a quantum dot. The squares indicate the ITGF results for fixed μ . The solid line indicates the GP result for fixed N . Corresponding ED results are shown as dashed lines. Note the broken π periodicity in the flux of the ED results at fixed N that is restored as L increases, similar to the EQD case. This again is a result of broken particle-hole symmetry. (b) Corresponding particle numbers in each ensemble. The discontinuities in the current when μ is fixed occur when the particle number jumps.

As verified extensively in this chapter, the persistent current in both SCQD and EQD geometries without interactions can be calculated using imaginary-time green's functions. These are used as the input to the Hirsch-Fye impurity QMC algorithm discussed in Chap. 2. Further details of calculating the effects of the Coulomb interaction in the dot are given in the next chapter.

Chapter 4

Persistent Current Through Interacting Quantum Dots

Chapter 2 described the general framework of the Hirsch-Fye QMC algorithm, emphasizing the role of the impurity green's function g_{dd} . As discussed in Chap. 3, the persistent current can be calculated from the correlations between adjacent sites in the ring, g_{d1} and g_{1d} in the case of the EQD, g_{01} and g_{10} in the case of the SCQD, for instance. These correlation functions can also be determined in the interacting case through the framework described in Chap. 2. The first section of this chapter describes the relevant extensions to the Monte Carlo algorithm. The second section describes the results obtained to date in comparison with other calculations of the persistent current in interacting systems.

4.1 Calculating the Current in the Hirsch-Fye Algorithm

Evaluating the necessary green's functions in the Hirsch-Fye framework is straightforward using the Dyson equations (2.27) and (2.28) that relate the full green's function at different auxiliary spin configurations $\{\phi_\ell\}$ and $\{\phi'_\ell\}$. Given the effective time-dependent potentials V and V' generated by these two configurations, the Dyson equations are

$$g' = g + (g - I)(e^{V'-V} - I)g' \quad (2.27)$$

$$g' = g + (g' - I)(1 - e^{V-V'})g \quad (2.28)$$

These are the full $LL_\tau \times LL_\tau$ matrices containing information about all pairwise correlations in the system ($g_{ij}(\tau_\ell, \tau_{\ell'}) = \langle T \hat{c}_i(\tau_\ell) \hat{c}_j^\dagger(\tau_{\ell'}) \rangle$). The spin index has again been suppressed since there are no spin-flip processes in the Ander-

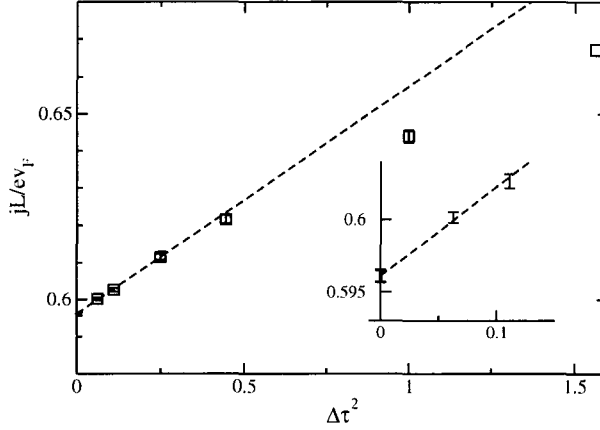


Figure 4.1: Extrapolation of the persistent current to $\Delta\tau = 0$. Results shown are the raw persistent current of the system described in Fig. 4.2 for the flux $\alpha = 0.4$, with $\beta = 20$ and $U = 2$. The dashed line is a linear fit to the data, and the point at $\Delta\tau^2 = 0$ shows the estimated current and error bars. The inset shows a close up of the extrapolation.

son model. While the Hirsch-Fye algorithm requires only the impurity green's function g_{dd} to perform the Monte Carlo sampling of the auxiliary field configurations, we can calculate the other green's functions of interest as well by taking matrix elements of the above equations.

$$g'_{dj} = g_{dj} + (g'_{dd} - I)(I - e^{V-V'})g_{dj} \quad (4.1)$$

$$g'_{jd} = g_{jd} + g_{jd}(e^{V'-V} - I)g'_{dd} \quad (4.2)$$

$$g'_{jj'} = g_{jj'} + g_{jd}(e^{V'-V} - I)g'_{dj} \quad (4.3)$$

These allow us to calculate the additional green's functions without inverting any additional matrices

$$g'_{dj} = A_{dj}g_{dj} \quad A_{dj} = I + (g'_{dd} - I)(I - e^{V-V'}) \quad (4.4)$$

$$g'_{jd} = g_{jd}A_{jd} \quad A_{jd} = I + (e^{V'-V} - I)g'_{dd} \quad (4.5)$$

$$g'_{jj'} = g_{jj'} + g_{jd}A_{jj'} \quad A_{jj'} = (e^{V'-V} - I)g'_{dj} \quad (4.6)$$

Moreover, when the auxiliary spin configurations differ only by a single flip ($\phi_s \rightarrow \phi'_s$), updating these green's functions is even more trivial than updating the impurity green's function.

$$g'_{dj}(\tau_\ell, \tau_{\ell'}) = g_{dj}(\tau_\ell, \tau_{\ell'}) + (g'_{dd}(\tau_\ell, \tau_s) - \delta_{\ell s})(1 - e^{V_s - V'_s})g_{dj}(\tau_s, \tau_{\ell'}) \quad (4.7)$$

$$g'_{jd}(\tau_\ell, \tau_{\ell'}) = g_{jd}(\tau_\ell, \tau_{\ell'}) + g_{jd}(\tau_\ell, \tau_s)(e^{V'_s - V_s} - 1)g'_{dd}(\tau_s, \tau_{\ell'}) \quad (4.8)$$

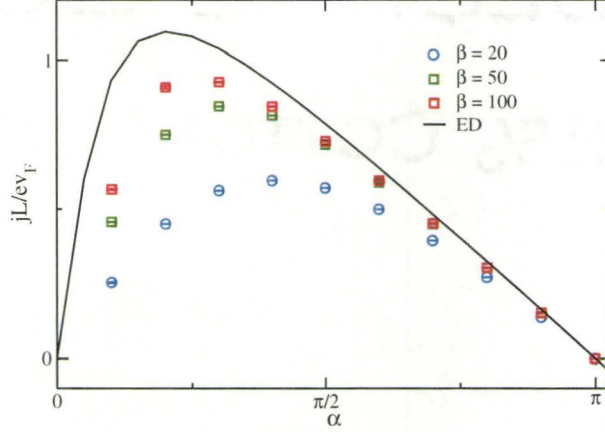


Figure 4.2: Persistent current for an EQD in a $L = 16$ site ring with $t' = 0.5$, $U = 2$, and $\epsilon_d = -1$. The solid line is the current calculated by full, many-body ED courtesy of E. S. Sørensen. Monte Carlo results at $\beta = 20, 50$, and 100 evolve towards the $T = 0$ result.

$$g'_{jj'}(\tau_\ell, \tau_{\ell'}) = g_{jj'}(\tau_\ell, \tau_{\ell'}) + g_{jd}(\tau_\ell, \tau_s)(e^{V'_s - V_s} - 1)g'_{dj}(\tau_s, \tau_{\ell'}) \quad (4.9)$$

These matrix operations are $O(L_\tau^2)$ and must be performed at each Monte Carlo sweep. While the green's functions required for calculating the current in the EQD geometry (g_{d1} and g_{1d}) can be calculated directly from the impurity green's function, calculating the current in the SCQD geometry requires six additional green's functions to be calculated: g_{d0} , g_{0d} , g_{d1} , g_{1d} , g_{01} , and g_{10} .

4.2 Results

The only systematic error present in the Hirsch-Fye QMC algorithm stems from the Trotter decomposition of the partition function. For small $\Delta\tau$, the error should be of order $\Delta\tau^2$. A fully accurate estimate of any quantity thus involves running with successively larger numbers of time slices L_τ looking for behaviour linear in $\Delta\tau^2$ in order to extrapolate to the $\Delta\tau = 0$ limit. An example of such an extrapolation is shown in Fig. 4.1. Clearly this extrapolation becomes more difficult as β increases; it is also sensitive to the strength of the interaction U , becoming more difficult as U increases.

Few exact results for the persistent current in the interacting Anderson model at finite temperature exist in order to check the results of this algorithm in detail. Two checks, however, have been performed for the EQD case. Notably, all determinant ratios R (see Eq. (2.35)) calculated have been real and positive, that is, there has been no fermionic sign problem.

Figure 4.2 shows results for a $L = 16$ ring with $t' = 0.5$, $U = 2$ at the

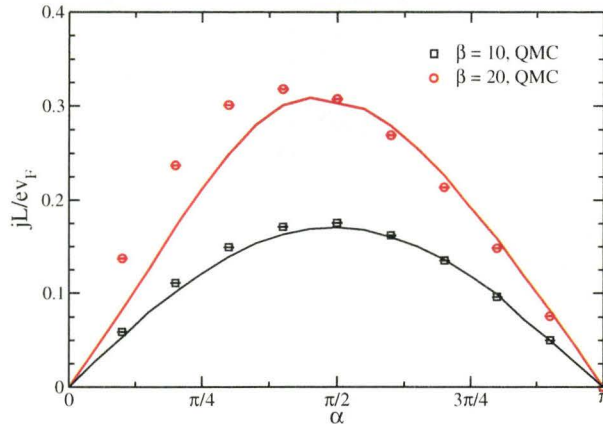


Figure 4.3: Persistent current for an EQD in a $L = 8$ site ring with $t' = 0.2$, $U = 0.5$, and $\epsilon_d = -0.25$. The solid lines are perturbative results reported by Aligia [22]. The symbols are QMC results at $\beta = 10$ and 20.

particle-hole symmetric point $\epsilon_d = -1$. The solid line was calculated by exact diagonalization of the many-body Hamiltonian (3.11), provided by Erik Sørensen. Due to computational limitations, calculations have not been performed at low enough temperatures to fully recover the $T = 0$ result, however the finite temperature results are converging towards the zero temperature results. In particular, the finite temperature results reproduce the zero temperature slope of the current near $\alpha = \pi$.

Figure 4.3 shows results for a $L = 8$ ring with $t' = 0.2$, $U = 0.5$ again at the particle-hole symmetric point $\epsilon_d = -0.25$. The Monte Carlo results are compared here with results for the interacting Anderson model due to Aligia [22] calculated with a self-consistent perturbative approach, accurate to second order in U . The agreement is not perfect, particularly for low flux, but the temperature dependence is of the correct order of magnitude, lending good confidence to the QMC results.

Coulomb Blockade

In order to observe an effect solely due to the presence interactions, the persistent current on a 16-site EQD ring was calculated while varying the impurity site energy ϵ_d . Results are shown in Fig. 4.4. The current peaks at $\epsilon_d = 0$ as it would in the non-interacting system, but it also peaks at $\epsilon_d = -U$ due to the Coulomb interactions on the dot. The peaks are similar to the Coulomb blockade peaks in similar plots of the conductance through an embedded quantum dot. Further checks of the algorithm have not been possible due to time limitations.

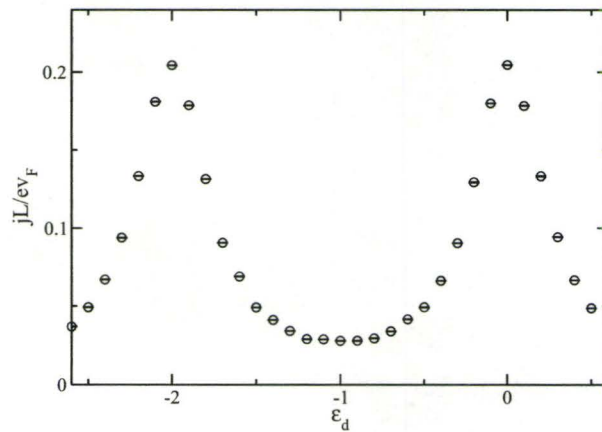


Figure 4.4: Persistent current for an EQD in a 16-site ring with $t' = 0.2$, $U = 2$, and $\beta = 20$ as a function of ϵ_d . The current peaks near $\epsilon_d = 0$ and $\epsilon_d = -U$ and is suppressed between these values, an effect reminiscent of the Coulomb blockade that is not present in the non-interacting system. The results shown have not been extrapolated to $\Delta\tau = 0$ ($\Delta\tau^2 = 0.0625$).

Chapter 5

Conclusions and Perspectives

5.1 Conclusions

This thesis has demonstrated the feasibility of calculating persistent currents in rings coupled to quantum dots using the Hirsch-Fye impurity Quantum Monte Carlo algorithm. The fortunate lack of a fermionic sign problem makes this a powerful technique for numerically calculating exact results over a wide range of parameter space at finite temperatures. Though only calculations in the EQD geometry have been verified due to time constraints, there are no difficulties foreseen in performing calculations in the SCQD geometry.

5.1.1 Accessible Parameter Regimes

The primary computational challenge for this algorithm lies in simulating low temperatures since the algorithmic complexity effectively scales as $O(\beta^3)$. The error due to the Trotter decomposition is also sensitive to the strength of the interaction U , consequently simulating Kondo impurities is computationally more difficult. While extracting the ground state properties of any large system size will be challenging, low temperature physics should be accessible. Although the algorithm is intrinsically insensitive to the size of the system L , the shrinking of the mesoscopic gap as $L \rightarrow \infty$ in turn requires simulations to be run lower temperatures.

In the broader scope, the algorithm should be adaptable to many modifications of the Hamiltonian. It should be straightforward to include the effects of asymmetric couplings, static disorder in the ring, Zeeman splitting of the energy levels in the dot, or Aharonov-Casher effects [9]. The possibility of investigating multi-channel models has not been considered in detail. Including multiple impurities (with on-site Coulomb interactions) or interactions between the conduction electrons will introduce a fermionic sign problem away from particle-hole symmetric points [54], making such calculations difficult.

Quantum Monte Carlo calculations in the Hubbard model, however, can be performed in some parameter regimes despite the sign problem, so it is possible that some relevant calculations could be performed in such cases as well.

5.2 Further Work

Having demonstrated that the technique is feasible and generates correct results, there are a variety of worthwhile projects to be undertaken. Three of them are discussed below.

- The Kondo problem has historically acted as an important context for developing ideas of scaling and the renormalization group. As pointed out by Simon and Affleck [5], the persistent current should be a universal function at $T = 0$ of the flux α and of L/ξ_K (modulo parity effects). At finite temperature, the current should also be a function of T/T_K

$$jL = f(\alpha, L/\xi_K, T/T_K). \quad (5.1)$$

It should be feasible to confirm this scaling relation, verifying as well the controversial prediction that the current is suppressed in the SCQD case as $L \gg \xi_K$.

- Experiments measuring the persistent current are extremely difficult to perform. It has been proposed [7] that by weakly coupling the ring to a particle-bath, it may be more feasible to observe electrons tunnelling into and out of the ring as a function of the flux. If this signal has a strong finite-size dependence, it may provide another means of indirectly detecting the screening cloud. While the total number of particles is not directly accessible to this algorithm, it may be possible to determine $N(\alpha, L/\xi_K, T/T_K)$ by means of a sum rule.
- Although it has not been emphasized in this thesis, a great deal of theoretical work has been devoted to understanding the conductance through quantum dots coupled to infinite quantum wires. Since the Hirsch-Fye algorithm gives information about the dynamics of the system as well, it may be possible to calculate the conductance directly in the thermodynamic limit either with a Kubo formula, or by looking for a term proportional to $|\omega_n|$ in the imaginary-time impurity green's function $g_{dd}(i\omega_n)$ [44].

Bibliography

- [1] D. Goldhaber-Gordon, J. Göres, M. A. Kastner, H. Shtrikman, D. Mahalu, and U. Meirav. Kondo effect in a single-electron transistor. *Nature*, 391:156, 1998.
- [2] S. M. Cronenwett, T. H. Oosterkamp, and L. P. Kouwenhoven. A tunable Kondo effect in quantum dots. *Science*, 281:540, 1998.
- [3] J. Nygard, D. H. Cobden, and P. E. Lindelof. Kondo physics in carbon nanotubes. *Nature*, 408:342, 2000.
- [4] E. S. Sørensen and I. Affleck. Scaling theory of the Kondo screening cloud. *Phys. Rev. B*, 53:9153, 1996.
- [5] I. Affleck and P. Simon. Detecting the kondo screening cloud around a quantum dot. *Phys. Rev. Lett.*, 86:2854, 2001.
- [6] P. Simon and I. Affleck. Persistent currents through a quantum dot. *Phys. Rev. B*, 64:085308, 2001.
- [7] I. Affleck. Personal Communication.
- [8] M. Büttiker and C. A. Stafford. Charge transfer induced persistent current and capacitance oscillations. *Phys. Rev. Lett.*, 76:495, 1996.
- [9] H.-P. Ecker, H. Johannesson, and C.A. Stafford. Kondo resonance in a mesoscopic ring coupled to a quantum dot: Exact results for the Aharonov-Bohm-Casher effects. *Phys. Rev. Lett.*, 87:016602, 2001.
- [10] E. S. Sørensen and I. Affleck. Kondo screening cloud around a quantum dot: Large-scale numerical results. *Phys. Rev. Lett.*, 94:086601, 2005.
- [11] J. E. Hirsch and R. M. Fye. Monte Carlo method for magnetic impurities in metals. *Phys. Rev. Lett.*, 56:2521, 1986.
- [12] A. C. Hewson. *The Kondo problem to heavy fermions*. Cambridge University Press, Cambridge, 1993.

- [13] I. Affleck. Conformal field theory approach to the kondo effect. *Acta Phys. Polon.*, B26:1869, 1995.
- [14] W. G. van der Wiel, S. De Franceschi, T. Fujisawa, J. M. Elzerman, S. Tarucha, and L. P. Kouwenhoven. The Kondo effect in the unitary limit. *Science*, 289:2105, 2000.
- [15] V. Barzykin and I. Affleck. Screening cloud in the k-channel Kondo model: Perturbative and large-k results. *Phys. Rev. B*, 57:432, 1998.
- [16] P. Coleman. Local moment physics in heavy electron systems. In F. Mancini, editor, *Lectures on the Physics of Highly Correlated Electron Systems VI*, page 79. American Institute for Physics, New York, 2002. also available as cond-mat/0206003.
- [17] D. Mailly, C. Chapelier, and A. Benot. Experimental observation of persistent currents in gaas-algaas single loop. *Phys. Rev. Lett.*, 70:2020, 1993.
- [18] V. Ferrari, G. Chiappe, E. V. Anda, and M. A. Davidovich. Kondo resonance effect on persistent currents through a quantum dot in a mesoscopic ring. *Phys. Rev. Lett.*, 82:5088, 1999.
- [19] K. Kang and S.C. Shin. Mesoscopic Kondo effect in an Aharonov-Bohm ring. *Phys. Rev. Lett.*, 85:5619, 2000.
- [20] S. Y. Cho, K. Kang, C. K. Kim, and C.-M. Ryu. Spin fluctuation and persistent current in a mesoscopic ring coupled to a quantum dot. *Phys. Rev. B*, 64:033314, 2001.
- [21] H. Hu, G-M. Zhang, and L. Yu. Mesoscopic Kondo screening effect in a single-electron transistor embedded in a metallic ring. *Phys. Rev. Lett.*, 86:5558, 2001.
- [22] A. A. Aligia. Persistent currents in mesoscopic rings with a quantum dot. *Phys. Rev. B*, 66:165303, 2002.
- [23] E. V. Anda, C. Busser, G. Chiappe, and M. A. Davidovich. Kondo effect and persistent currents in a mesoscopic ring: numerically exact results. *Phys. Rev. B*, 66:165303, 2002.
- [24] Y. Meir, N. S. Wingreen, and P. A. Lee. Low-temperature transport through a quantum dot: The Anderson model out of equilibrium. *Phys. Rev. Lett.*, 70:2601, 1993.
- [25] S. Hershfield, J. H. Davies, and J. W. Wilkins. Probing the Kondo resonance by resonant tunneling through an Anderson impurity. *Phys. Rev. Lett.*, 67:3720, 1991.

- [26] J. Schmid, J. Weis, K. Eberl, and K. von Klitzing. A quantum dot in the limit of strong coupling to reservoirs. *Physica B*, 256-258:182, 1998.
- [27] S. Datta. *Electronic Transport in Mesoscopic Systems*. Cambridge University Press, Cambridge, 1994.
- [28] F. D. M. Haldane. Scaling theory of the asymmetric Anderson model. *Phys. Rev. Lett.*, 40:416, 1978.
- [29] D. Goldhaber-Gordon, J. Göres, M. A. Kastner, H. Shtrikman, D. Mahalu, and U. Meirav. From the Kondo regime to the mixed-valence regime in a single-electron transistor. *Phys. Rev. Lett.*, 81:5225, 1998.
- [30] S. Sasaki, S. De Franceschi, J. M. Elzerman, W. G. van der Wiel, M. Eto, S. Tarucha, and L. P. Kouwenhoven. Kondo effect in an integer-spin quantum dot. *Nature*, 405:764, 2000.
- [31] N. J. Craig, J. M. Taylor, E. A. Lester, C. M. Marcus, M. P. Hanson, and A. C. Gossard. Tunable nonlocal spin control in a coupled-quantum dot system. *Science*, 304:565, 2004.
- [32] A. W. Holleitner, R. H. Blick, A. K. Huttel, K. Eberl, and J. P. Kotthaus. Probing and controlling the bonds of an artificial molecule. *Science*, 297:70, 2002.
- [33] F. Bloch. Josephson effect in a superconducting ring. *Phys. Rev. B*, 2:109, 1970.
- [34] M. Büttiker, Y. Imry, and R. Landauer. Josephson behavior in small normal one-dimensional rings. *Phys. Lett. A*, 96:365, 1983.
- [35] Y. Imry. *Introduction to mesoscopic physics*. Oxford University Press, Oxford, second edition, 2002.
- [36] H. F. Cheung, Y. Gefen, E. K. Riedel, and W. H. Shih. Persistent currents in small one-dimensional metal rings. *Phys. Rev. B*, 37:6050, 1988.
- [37] L. P. Lévy, G. Dolan, J. Dunsmuir, and H. Bouchiat. Magnetization of mesoscopic copper rings: Evidence for persistent currents. *Phys. Rev. Lett.*, 64:2074, 1990.
- [38] V. Chandrasekhar, R. A. Webb, M. J. Brady, M. B. Ketchen, W. J. Gallagher, and A. Kleinsasser. Magnetic response of a single, isolated gold loop. *Phys. Rev. Lett.*, 67:3578, 1991.

- [39] B. Reulet, M. Ramin, H. Bouchiat, and D. Mailly. Dynamic response of isolated Aharonov-Bohm rings coupled to an electromagnetic resonator. *Phys. Rev. Lett.*, 75:124, 1995.
- [40] E. M. Q. Jariwala, P. Mohanty, M. B. Ketchen, and R. A. Webb. Diamagnetic persistent current in diffusive normal-metal rings. *Phys. Rev. Lett.*, 86:1594, 2001.
- [41] W. Rabaud, L. Saminadayar, D. Mailly, K. Hasselbach, A. Benot, and B. Etienne. Persistent currents in mesoscopic connected rings. *Phys. Rev. Lett.*, 86:3124, 2001.
- [42] R. Deblock, R. Bel, B. Reulet, H. Bouchiat, and D. Mailly. Diamagnetic orbital response of mesoscopic silver rings. *Phys. Rev. Lett.*, 89:206803, 2002.
- [43] A. A. Zvyagin and P. Schlottmann. Finite-size effects in a metallic multichannel ring with Kondo impurity: Persistent currents and magnetoresistance. *Phys. Rev. B*, 54:15191, 1996.
- [44] I. Affleck and E. S. Sørensen. Fermi liquid theory for the side-coupled quantum dot. unpublished.
- [45] R. M. Fye and J. E. Hirsch. Monte carlo study of the symmetric Anderson-impurity model. *Phys. Rev. B*, 38:433, 1988.
- [46] A. Georges, G. Kotliar, W. Krauth, and M. J. Rozenberg. Dynamical mean-field theory of strongly correlated fermion systems and the limit of infinite dimensions. *Rev. Mod. Phys.*, 68:13, 1996.
- [47] R. M. Fye and J. E. Hirsch. Quantum monte carlo study of the two-impurity Kondo hamiltonian. *Phys. Rev. B*, 40:4780, 1989.
- [48] M. Feldbacher, K. Held, and F. F. Assaad. Projective quantum monte carlo method for the Anderson impurity model and its application to dynamical mean field theory. *Phys. Rev. Lett.*, 93:136405, 2004.
- [49] F. F. Assaad. Quantum Monte Carlo methods on lattices: The determinantal approach. In J. Grotendorst, D. Marx, and A. Muramatsu, editors, *Quantum Simulations of Complex Many-Body Systems: From Theory to Algorithms*, volume 10, page 99. John von Neumann Institute for Computing, Jülich, 2002.
- [50] R. Blankenbecler, D. J. Scalapino, and R. L. Sugar. Monte Carlo calculations of coupled boson-fermion systems. *Phys. Rev. D*, 24:2278, 1981.

- [51] R. M. Fye. New results on Trotter-like approximations. *Phys. Rev. B*, 33:6271, 1986.
- [52] J. E. Hirsch. Discrete Hubbard-Stratanovich transformation for fermion lattice models. *Phys. Rev. B*, 28:4059, 1983.
- [53] J. E. Hirsch. Two-dimensional Hubbard model: Numerical simulation study. *Phys. Rev. B*, 31:4403, 1985.
- [54] J. Yoo, S. Chandrasekharan, R. K. Kaul, D. Ullmo, and H. U. Baranger. On the sign problem in the Hirsch-Fye algorithm for impurity problems. *J. Phys. A: Math. Gen.*, 38:10307, 2005.
- [55] A. O. Gogolin and N. V. Prokof'ev. Simple formula for the persistent current in disordered one-dimensional rings: Parity and interaction effects. *Phys. Rev. B*, 50(2):4921, 1994.